Tomography of time-bin entangled photons from a quantum dot

Philipp Aumann

Master thesis

Institute for Theoretical Physics
University of Innsbruck
Austria

August 1, 2017

Abstract

Quantum cryptography provides an unique way of communication by making use of quantum physical effects with the aim to enhance security. It can be implemented with the use of entangled photons. This work contains a theoretical model and simulations for an experiment that focuses on the creation of time-bin entangled photons. Within the experimental setup, light from a pulsed laser is directed on a quantum dot which subsequently emits photons. This quantum dot is a semiconductor nano structure that can be used as a quantum emitter. A statistic of coincidence counts can be extracted from the detection of the emitted photons. In post selection, the photons should preferably pairwise exhibit the time-bin encoded generalized Bell state. An effective quantum optical model is used to simulate the dynamics of the system. It is possible to estimate the coincidence counts of the detectors based on the theoretical model. The estimated values of the photon counts are the input of a tomographic method which gives the reconstructed density matrix of the photons as an output. In this way the results of the experiment can be proposed for various values of parameters that can be related to the configuration of the laser. If the theoretical model is successfully adjusted to the experimental results, it is possible to propose laser configurations for the experiment in order to enhance the quality of the photons. The fidelity between a bell state and the simulated density matrix are discussed within this work. Choices of parameters can be extracted for which the fidelity is suggested to be very large, such that this might lead to a noticeable enhancement compared to the fidelities achieved so far. The number of simulated coincidence counts, which is correlated to the potential number of created photons, and the fidelity, however, show a weak accordance when system parameters are varied. Therefore, the potential user of the system has to find a compromise between the number of photons and their proximity to the desired state.

Zusammenfassung [1]

Quantenkryptographie bietet eine einzigartige Art der Kommunikation indem quantenphysikalische Effekte ausgenutzt werden mit dem Ziel die Sicherheit zu erhöhen. Diese Verschlüsslung kann mit verschränkten Photonen implementiert werden. Diese Arbeit beinhaltet ein theoretisches Modell und Simulationen für ein Experiment, welches sich um die Erzeugung time-bin verschränkter Photonen dreht. Im experimentellen Aufbau wird Licht eines gepulsten Lasers auf einen Quantenpunkt gerichtet, welcher anschließend Photonen emittiert. Dieser Quantenpunkt ist eine Halbleiter-Nanostruktur welcher als Quantenemitter betrieben werden kann. Eine Statistik von Koinzidenzmessungen kann aus der Detektion der emittierten Photonen gewonnen werden. In nachträglicher Selektion sollten die Photonen paarweise möglichst den time-bin kodierten verallgemeinerten Bellzustand aufweisen. Ein effektives quantenoptisches Modell wird benutzt um die Dynamik des Systems zu simulieren. Basierend auf dem theoretischen Modell ist es möglich die Koinzidenzmessungen der Detektoren abzuschätzen. Die abgeschätzten Werte der Photonen-Messungen dienen als Eingabe einer tomographischen Methode, welche die rekonstruierte Dichtematrix der Photonen als Ausgabe hat. Somit können die Ergebnisse des Experiments für verschiedene Werte von Parametern, welche mit Lasereinstellungen in Verbindung gebracht werden können, vorgeschlagen werden. Falls das theoretische Modell erfolgreich an die experimentellen Ergebnisse angepasst ist, ist es möglich Lasereinstellungen für das Experiment vorzuschlagen um die Qualität der Photonen zu erhöhen. Die Fidelity zwischen einem Bellzustand und der simulierten Dichtematrix werden in dieser Arbeit diskutiert. Wahlmöglichkeiten für Parameter, für welche die Fidelity als sehr hoch vorgeschlagen wird, können entnommen werden. Dies könnte zu einer merkbaren Verbesserung im Vergleich zu bisher erreichten Fidelitys führen. Die Anzahl der simulierten Koinzidenzmessungen, welche in Verbindung mit der potentiellen Anzahl von erzeugten Photonen steht, und die Fidelity weisen allerdings eine geringe Übereinstimmung auf wenn Systemparameter variiert werden. Somit muss der mögliche Nutzer des Systems einen Kompromiss zwischen der Anzahl von Photonen und deren Nähe zum gewünschten Zustand finden.

---

[1] This is the German version of the abstract. Apart from the acknowledgements (“Danksagungen”), the rest of the content is given in English.

Danksagungen [2]

Viele Personen haben mich während meines Studiums und während dem Entstehen dieser Masterarbeit begleitet und unterstützt.
Ich möchte mich bei Professor Helmut Ritsch für seine Betreuung dieser Masterarbeit bedanken. Durch seine studentennahe Betreuung habe ich mich sehr wohl gefühlt. Diese Studentennähe und Herzlichkeit wirkt sich auch positiv auf die Atmosphäre in der gesamten Arbeitsgruppe aus. Ich durfte eine sehr intensive und lehrreiche Betreuung genießen.
Herzlich bedanken möchte ich mich auch bei Laurin Ostermann, der sich nicht nur die Mühe gemacht hat, meine Arbeit zur Korrektur zu lesen sondern der auch auf meine zahlreichen Fragen eingegangen ist und sich für mich Zeit genommen hat.
Eure Anmerkungen und Formulierungsvorschläge haben zu der Arbeit beigetragen.
Mein Dank geht auch an die weiteren Mitarbeiter der Arbeitsgruppe. Zu diesen zählen Sebastian (welcher, als mein Schreibtischnachbar und gruppeninterner Ansprechpartner für Probleme der Informatik, viele Fragen abbekommen hat), Farokh, David, Artur, Stefan, Valentin und Daniela, sowie die ehemaligen Mitglieder Claudiu und Francesco. Mit euch durfte ich auch über die physikalischen Diskussionen hinaus, Unterhaltungen über Bergsport führen, am Adventskalender basteln oder zahlreiche Mittags- und Kaffeepausen genießen.
Herzlich möchte ich mich bei meinen Eltern Ulrich und Herta bedanken. Ihr habt mich in allen Lebenslagen unterstützt und mir ermöglicht meine Ziele zu erfüllen. Was ich euch darüber hinaus verdanke und was ihr in eure Kinder investiert habt würde sicherlich den Rahmen dieser kurzen Danksagungen sprengen.
Vielen Dank an Lluis, mit dem ich über viele Dinge diskutieren konnte und mit dem ich auf spaßige Unternehmungen zurückblicken darf und Jorge und Andrea mit denen ich einige spaßige Mittagspausen und schöne Zeiten verbringen durfte.
Viel Spaß und eine tolle Zeit hatte ich während meines Studiums auch mit meinen Mitbewohnern Michael, Paul, Lukas und Manuel, sowie meinen ehemaligen Mitbewohnern Jan und Hubertus. Vielen Dank für die zahlreichen Diskussionen und vielen erfrischenden Unternehmungen die wir zusammen gehabt haben und bei denen ich abschalten und mich verausgaben konnte. Schöne Zeit durfte ich auch mit Harry, Fabian, Christoph, Jonas, Petra, Philipp und vielen weiteren tollen Menschen haben, die hier nicht alle namentlich erwähnt werden. Vielen Dank für eure Begleitung.

---

[2] The acknowledgements are given in German.

Contents

Chapter 1

Introduction

The experiment [1, 2, 3] that is addressed in this master thesis explores the possibility to prepare photons in an entangled state in terms of time-bin encoding using a quantum dot. Quantum dots can be used to realize quantum confinement in all three spatial dimensions by exploiting properties of semiconductor materials. In our context, the exhibition of discrete energy levels is an important property of the quantum dot. We denote two of them by “exciton" and “biexciton" and describe the quantum dot system as a three level system together with the ground state. In the experiment, these levels are probed by light from a pulsed laser in order to create photons in time-bin entangled states. The time-bin encoding can be used to realize qubits and is a promising foundation for the implementation of quantum communication. This kind of communication uses the properties of quantum physics to ensure unique security standards. However, quantum communication also faces specific difficulties due to potentially strongly limited stabilities of quantum channels. The time-bin encoding exhibits high stability within optical fibres [4]. Quantum dots and time-bin encoding are treated in chapter 2 of this work.

The experiment has been complemented with theoretical support. Theoretical studies have been presented in the latest publication [1] together with experimental results. This master thesis extends the theoretical studies with the simulation of the outcome of the experiment and a subsequent discussion.

Chapter 3 covers the model that is used to describe the experiment from a theoretical viewpoint. It contains the derivation of a Hamiltonian that is similar to the one in the project's last publication [1]. Beyond that, an overview over several decoherence mechanisms is given.

A density matrix can be reconstructed from the detection of the photon's which are emitted by the quantum dot. The goal of this work is to provide a possibility to propose the reconstructed density matrix from a theoretical viewpoint by simulating the system's dynamics with the use of the already existing quantum optical model. The tomographic method [5, 6] that is used for this purpose is presented in chapter 4. This chapter also contains a calculation that is done in order to estimate the photon counts at the detector. These estimated values are the input of the tomographic reconstruction method.

The results of this work are presented in chapter 5. The fidelity between the simulated density matrix and a bell state is given. The theoretical studies propose choices of parameters that will lead to high fidelities.

Chapter 2

Experiment

The fundamental components of the experiment that is discussed within this work are a pulsed laser that addresses a self-assembled InAs quantum dot, a bulk interferometer and detectors. A more detailed discussion about the experiment can be found in the project's publications [1, 2, 3]. This chapter covers a short introduction to quantum dots and time-bin entanglement, which are underlying concepts that are used within this work, followed by a description of the experimental setup.

2.1 Quantum Dots

A crucial property of quantum dots is their exhibition of discrete energy levels. The following discussion gives a short introduction to the concept of discrete energy levels in semiconductors. This is followed by an introduction to the idea of quantum confinement as a further characteristic of a quantum dot.

2.1.1 Excitons

The electron energy spectrum of a semiconductor contains the lower valence and the higher conduction band which are separated by an energy gap. This can be discussed in the context of non-interacting electrons (or an averaged interaction between electrons). Adding a basic discussion of excitations and interaction within this framework can lead to a first notion of the so called "Exciton" which plays an important role in our investigation of a quantum dot. Within this subsection we will follow lecture notes of Manfred Sigrist [7] very closely up to most of the notation. The Hamiltonian for a semiconductor with Coulomb interaction between the electrons can be written in second quantization as

$$\hat{H} = \underbrace{\sum_{\vec{k},s} \epsilon_{v,\vec{k}} \hat{c}^\dagger_{v,\vec{k},s} \hat{c}_{v,\vec{k},s}}_{\text{valence band}} + \underbrace{\sum_{\vec{k},s} \epsilon_{c,\vec{k}} \hat{c}^\dagger_{c,\vec{k},s} \hat{c}_{c,\vec{k},s}}_{\text{conduction band}} + \underbrace{\sum_{s,s'} \int d^3r d^3r' \hat{\Psi}^\dagger_s(\vec{r}) \hat{\Psi}^\dagger_{s'}(\vec{r'}) \frac{e^2}{|\vec{r} - \vec{r'}|} \hat{\Psi}_{s'}(\vec{r'}) \hat{\Psi}_s(\vec{r})}_{\text{electron - electron interaction}}, \tag{2.1}$$

where $\hat{c}^\dagger_{v,\vec{k},s}$ ($\hat{c}_{v,\vec{k},s}$) creates (annihilates) an electron in the valence band with energy $\epsilon_{v,\vec{k}}$, with spin s and wave vector $\vec{k}$. $\hat{c}^\dagger_{c,\vec{k},s}$ ($\hat{c}_{c,\vec{k},s}$) creates (annihilates) an electron in the conduction band with energy $\epsilon_{c,\vec{k}}$, with spin s and wave vector $\vec{k}$.

$\hat{\Psi}_s(r)$ denotes the field operator with

$$\hat{\Psi}_s(\vec{r}) = \sum_{\substack{n=v,c \\ \vec{k}}} \Psi_{n,\vec{k}}(\vec{r}) \hat{c}_{n,\vec{k},s}, \tag{2.2}$$

where the wave function $\Psi_{n,\vec{k}}(\vec{r})$ is given by

$$\Psi_{n,\vec{k}}(\vec{r}) = \frac{1}{\sqrt{\Omega}} e^{i\vec{k}\vec{r}} u_{n,\vec{k}}(\vec{r}). \tag{2.3}$$

Ω denotes the volume of the system and $u_{n,\vec{k}}(\vec{r})$ is the Bloch function.
The state of a filled valence and empty conduction band is the ground state of the basic two-band model

$$|g\rangle := \prod_{\vec{k},s} \hat{c}^{\dagger}_{v,\vec{k},s} |0\rangle. \tag{2.4}$$

The most basic excitation is exciting an electron to the conduction band which leaves a "hole" in the valence band:

$$|\vec{k}+\vec{q}, s'; \vec{k}, s\rangle := \hat{c}^{\dagger}_{c,\vec{k}+\vec{q},s'} \hat{c}_{v,\vec{k},s} |g\rangle. \tag{2.5}$$

In a more general form this excitation with fixed spin and fixed momentum transfer $\vec{q}$ can be written as

$$|\psi_q\rangle = \sum_{\vec{k}} A(\vec{k}) |\vec{k}+\vec{q}, s'; \vec{k}, s\rangle. \tag{2.6}$$

Applying the bra $\langle \vec{k}+\vec{q}, s'; \vec{k}, s|$ to the stationary Schrödinger equation,

$$\hat{H}|\psi_q\rangle = (E_0 + E_q)|\psi_q\rangle,$$

leads to the following equation:

$$\sum_{\vec{k}'} \langle \vec{k}+\vec{q}, s'; \vec{k}, s| \; \hat{H} \; A(\vec{k}') |\vec{k}'+\vec{q}, s'; \vec{k}', s\rangle = (E_0 + E_q) A(\vec{k}). \tag{2.7}$$

In the following, the discussion focuses on the $\vec{k}$ and $\vec{k}'$ around 0 (the center of the Brillouin zone) and the case of small $|\vec{q}|$. This is legitimate for a material with a direct band gap at $\vec{k} = 0$ and small excitation energies. The approximation can be formulated as $\vec{k}' \approx \vec{k} \approx \vec{k} + \vec{q}$. In this sense, the underlying literature (see reference [7] for more details) sketches a derivation so that equation 2.7 becomes

$$(\epsilon_{c,\vec{k}+\vec{q}} - \epsilon_{v,\vec{k}} - E_q) A(\vec{k}) - \sum_{\vec{k}'} \frac{4\pi e^2}{\Omega \varepsilon |\vec{k} - \vec{k}'|^2} A(\vec{k}') = 0, \tag{2.8}$$

where ε is the dielectric constant of the semiconductor. This expression is limited to the regime where the above approximations about $\vec{k}, \vec{k}'$ and $\vec{q}$ are valid. With setting

$$\epsilon_{c,\vec{k}} = E_g + \frac{\hbar^2 \vec{k}^2}{2m_c} \tag{2.9}$$

and

$$\epsilon_{v,\vec{k}} = -\frac{\hbar^2 \vec{k}^2}{2m_v} \tag{2.10}$$

(E_g denotes the energy of the band gap, a direct energy gap is assumed at $\vec{k} = 0$ and the $\vec{k} \cdot \vec{p}$-approximation is used) one can find the following equation:

$$\left(\frac{-\hbar^2 \nabla^2}{2\mu} - \frac{e^2}{\varepsilon |\vec{r}|}\right) F(\vec{r}) = \left(E_{\vec{q}} - E_g - \frac{\hbar^2 \vec{q}^2}{2M}\right) F(\vec{r}) \tag{2.11}$$

with the definition

$$F(\vec{r}) := \frac{1}{\sqrt{\Omega}} \sum_k A(\vec{k}) e^{i\vec{k}\vec{r}}. \tag{2.12}$$

$\mu = \frac{\tilde{m}}{2}$ is the reduced mass with $\tilde{m} := m_c = m_v$ and $M = 2\tilde{m}$ the total mass. Equation 2.11 has the form of the Schrödinger equation of the hydrogen atom in relative coordinates. The latter equation can be written as [8]

$$\left(\frac{-\hbar^2 \nabla^2}{2\mu} - \frac{Ke^2}{|\vec{r}|}\right) \Psi_n(\vec{r}) = E_n \; \Psi_n(\vec{r}), \tag{2.13}$$

where $\vec{r}$ is the relative coordinate between the electron and proton of the hydrogen atom and $K = \frac{1}{4\pi\epsilon_0}$ with ϵ_0 being the dielectric constant of the vacuum. By solving this Schrödinger equation, the discrete energy spectrum of hydrogen can be found to be [8]

$$E_n = -\frac{\mu K^2 e^4}{2\hbar^2 n^2}. \tag{2.14}$$

The fact that equation 2.11 coincides with the form of the hydrogen atom's Schrödinger equation allows for formulating an analogy between an excited semiconductor and the hydrogen atom. The electron in the conduction band and the hole in the valence band play the role of electron and proton of the hydrogen atom, respectively. Just as we can find bound states with discrete energy levels forming the hydrogen atom, we can talk about the electron and hole forming a particle-like bound or quasiparticle called "exciton".
Comparing equation 2.11 and 2.13 and setting $K \to \frac{1}{\varepsilon}$ leads to

$$E_{\vec{q}} = E_g + \frac{\hbar^2 \vec{q}^2}{2M} - \frac{\mu e^4}{2\varepsilon^2 \hbar^2 n^2}. \tag{2.15}$$

These discrete energy levels can be associated with bound states and can be called excitons. A Quantum Dot consists of semiconductor material and provides us with the possibility to observe excitons. The states that are not considered within the above approximations (the ones for larger $\vec{k}$ and $\vec{q}$) contribute to an energy-continuum. This continuum can be interpreted as ionized excitons. Within the experiment that is described throughout this work another state plays a crucial role. This state lies energetically higher then the exciton that is being addressed. We call it a "biexciton" and interpret it as the bound state of two electrons and two holes.

2.1.2 Quantum Confinement

Excitons and biexcitons are not the only important features of a quantum dot. For the previous discussion of excitons, the material properties of a semiconductor has been considered and not the special properties of a quantum dot. Another crucial property of a quantum dot is that the energy gap can be engineered as energy levels

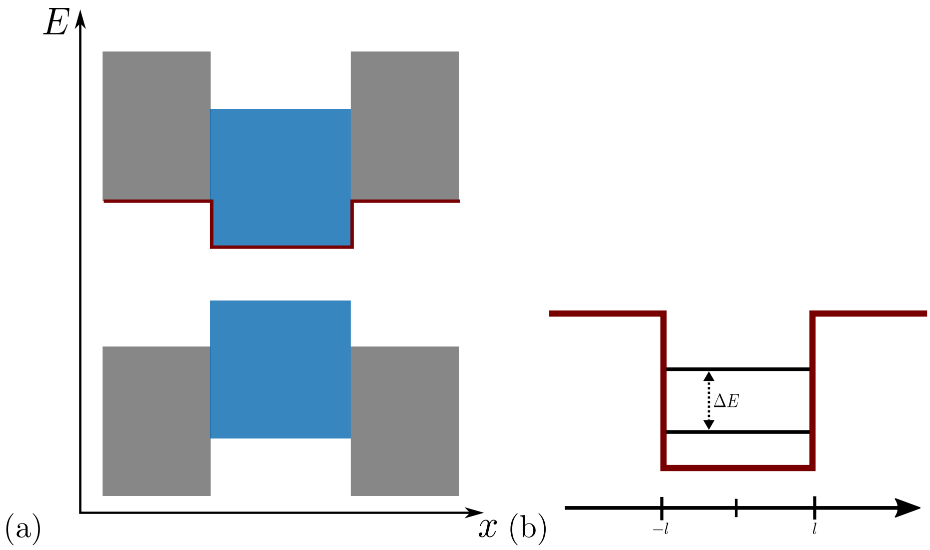

Figure 2.1: (a): Configuration of layers of two different semiconductors to implement a square well potential that leads to quantum confinement. A similar figure can be found in reference [9].
(b): Depiction of a square well potential that shows two discrete energy levels. A similar figure can be found in reference [8].

are discretized while the electrons are spatially confined. The degrees of freedom of the electrons and holes can be reduced by spatially confining them in all three dimensions. This is the procedure of “Quantum Confinement”. This subsection should be understood as a more general elaboration on quantum dots and not as a specific discussion regarding the experiment discussed in this thesis. Throughout this subsection we follow the presentation of quantum confinement in reference [9]. To reduce one spatial degree of freedom one might implement a quantum well potential along one direction. To realize this, layers of two different semiconductors can be aligned such that the energy bands are ordered along one direction as shown in figure 2.1a. The semiconductor under consideration is put in between two layers of an auxiliary semiconductor with a larger band gap. This results in an effective square well potential for the electrons in the conduction band. As depicted in figure 2.1b, such a potential exhibits discrete energy levels. The wave function for the ground state of a particle inside a square well potential can be written as

$$\Psi(x) = A\cos(qx) \tag{2.16}$$

for the area of the potential $[-l, l]$ [8]. A is a constant, $q = \sqrt{\frac{2m(V-|E|)}{\hbar^2}}$ with V being the depth of the potential, m being the mass of the electron and E the energy of the state. This wave function has two important properties:

1. It is static, i.e. $|\Psi|^2$ does not vary in time.
2. The expectation value of the momentum operator $\langle \hat{p}_x \rangle$ vanishes:

$$\langle \hat{p}_x \rangle = -A^2 \int_{-l}^{l} \mathrm{d}x \;\cos(qx)\; i\hbar\; \partial_x \cos(qx) = \frac{i\hbar A^2}{2} \int_{-l}^{l} \mathrm{d}x \sin(2qx) = 0.$$

Therefore it is legitimate to say that the electron exhibits no dynamics along the direction where it is effected by the potential and is confined in this respect. This

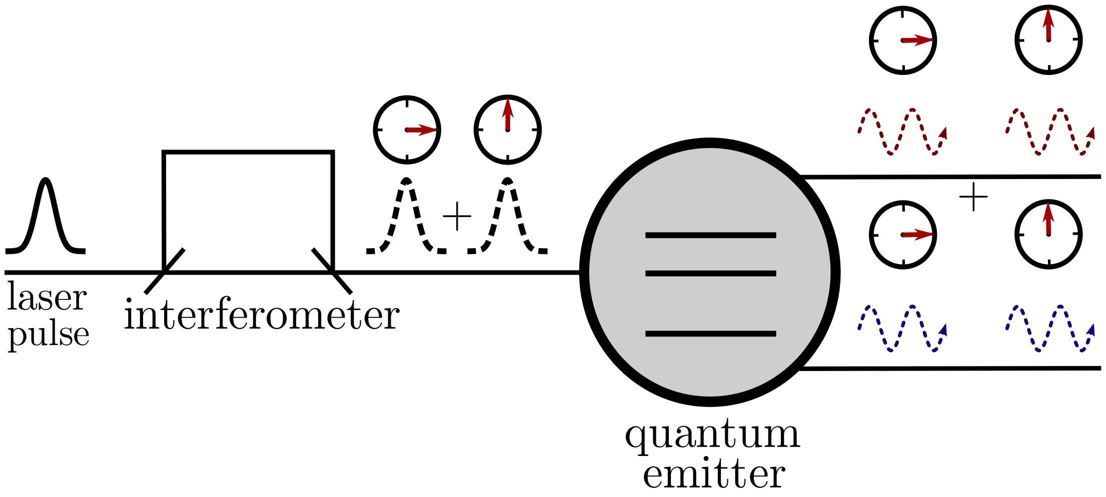

Figure 2.2: Scheme of the procedure to generate time-bin entangled photons. Similar schemes are contained in references [1, 2, 3]

however does not mean that the electron has no kinetic energy along this direction since $\langle \hat{p}_x^2 \rangle \neq 0$. Yet, if kept in the ground state, it exhibits no degree of freedom along the direction of the potential since it will stay in the static state $\Psi(x)$. This can be compared to a classical frictionless pendulum, which exhibits kinetic energy along the direction of oscillation, however the total momentum, which is averaged over one cycle, will be zero and the pendulum will simply remain in it's initial state. To achieve the discussed properties it is important that the full population stays in a single eigenstate of the system. While the previous discussion might be true for any eigenstate, practically the simplest approach is to cool down the whole system until only the ground state is occupied.

The energy of the ground state can be altered by varying the length of the layers. In this respect it is possible to engineer the band gap of the semiconductor.

If an effective potential is realized in all three dimensions, the electrons movement in any direction is restricted. In the case that all directions are blocked one can speak of a quantum dot.

2.2 Time-Bin Entanglement

There are various ways to implement qubits via photons. In our project we choose the time-bin encoding which we want to discuss in the following. The basic idea of time-bin encoding is to consider two different time slots (or time-bins) within a set-up and assign the logical $|0\rangle$ and $|1\rangle$ to this two time slots. These time windows could be seen as two distinct emission times of a quantum emitter, two different detection times at a photon detector or simply two timeframes of a photon propagating through a fiber. In our project all these different notions are applicable.

Compared to polarization encoding, the creation and encoding of time-bin qubits is more complex and technically more challenging. However they show great stability when propagating through a fiber [4].

To generate entanglement between two photons, they have to be prepared such that their time-bins are quantum correlated. Figure 2.2 schematically shows the procedure to generate time-bin entangled photons that has been chosen for our project.

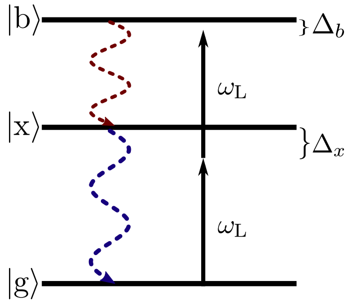

Figure 2.3: Level scheme of the quantum dot. $|b\rangle$, $|x\rangle$ and $|g\rangle$ refer to the biexciton, exciton and ground state. Δ_x and Δ_b are the detunings. Δ_x is the difference between the exciton energy level and the single photon energy and Δ_b is the difference between the biexciton energy level and the double photon energy. $\hbar$ is set to 1. Similar schemes can be found in references [1, 2, 3].

A laser pulse is send through an interferometer. This interferometer is unbalanced, which means the optical length of one arm is different from the other. The initial pulse is therefore split into two pulses, one that propagates through the long arm and the other one that propagates through the short arm. We label the pulses with “late” and “early”. They correspond to the two time-bins. It is important to note that within a quantum mechanical description, the photons that correspond to the first pulse are now in a superposition of being in the late and in the early pulse. In a descriptive way, one could say the single photons propagate through both arms simultaneously. Subsequently, the pulses excite a three level quantum emitter which decays by emitting photons of different frequencies. In general, the emission of the photons can take place at two different time slots, corresponding to the two pulses. The superposition of the early and late pulse is carried over to the emission times of the quantum emitter. This leads to a superposition of the photons being emitted in the early or late time bin. The aim of the experiment is to create emitted photons in the generalized Bell state: $|\Phi_\varphi\rangle = \frac{1}{\sqrt{2}}(|\mathrm{ee}\rangle + e^{i\varphi}|\mathrm{ll}\rangle)$. Where $|\mathrm{ee}\rangle$ ($|\mathrm{ll}\rangle$) means that a photon of the first and a photon of the second frequency is emitted in the early (late) time bin and φ denotes the phase. More precisely, the generalized Bell state is the desired outcome of the used tomographic method which involves post-selection.

2.3 Experimental Setup

This subsection gives a schematic overview of the setup of the experiment which is discussed throughout this thesis. More details can be found in the projects publications [1], [2], [3]. The first part of the experiment is schematically structured as depicted in figure 2.2 which shows the chosen procedure to generate time-bin entangled photon pairs. The quantum emitter in our case is a III/V self-assembled quantum dot [2]. We treat the quantum dot as a three level system that consists of a ground state (or vacuum in the quasi-particle language), an exciton and a biexciton state. This is an approximation since the system involves more states that could be addressed. However when filtering out one photon polarization the emission spectrum of a quantum dot which is discussed in reference [3] and [2] shows distinct peaks within a certain frequency range. These peaks correspond to the biexciton, the exciton, a trion and laser scattering. If the peak generated by the trion is small enough it is a good approximation to describe the quantum dot as a three level system. The direct single photon excitation from the ground state to the biexciton state is forbidden by selection rules. However it can be driven by a two-photon excitation, which is an excitation involving two photons at the same time. The sum of their energy is the energy of the desired transition (up to a detuning). A virtual intermediate level can be assigned to this process. The level scheme is depicted in figure 2.3.

The laser pulse is generated by a pulsed laser with subsequent pulse shaping. The shape of the laser will later be approximated to be Gaussian within our theoretical model. The length of the pulse can be varied.

As shown in figure 2.3, the quantum dot will emit a photon when the biexciton decays to the exciton state and another photon when the exciton decays to the ground state. These two photons show a difference in wavelength. They are analysed separately in distinct channels with analysis interferometers and subsequent detectors. Chapter 4 contains a closer look at this analysis. Altogether there are three interferometers: One analysis interferometer for each of the two photon channels and one interferometer that is used to generate the correlated early and late pulses (which is illustrated schematically in figure 2.2). These interferometers are implemented in one combined, so-called bulk interferometer [2].

Chapter 3

Theoretical Model

The aim of this work is to simulate the creation of entangled photons by using a quantum dot as a three level system. The corresponding experiment is described in chapter 2. From the numbers of simulated photon counts, we obtain the reconstructed density matrix of the photon pairs which are emitted by the quantum dot. The post-selective reconstruction process uses the tomographic method that is described in chapter 4. To be able to simulate the outcome, we make use of a simplified theoretical model that describes the system of the quantum dot and the laser embedded in an environment. This model was introduced in reference [1]. Within this chapter we want to give a short introduction to the theoretical toolkit used to describe open systems. This will be followed by a derivation of the system's Hamiltonian and a discussion of dissipative effects that are involved.

3.1 Open System Dynamics

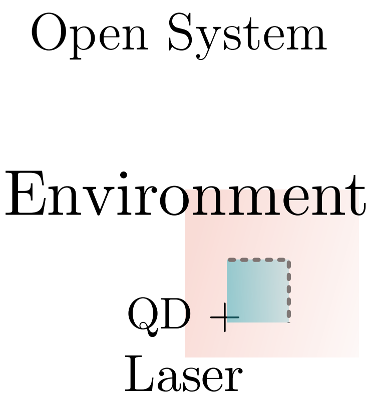

Figure 3.1: Conceptual separation between the quantum dot and laser as the "system" and the environment as "bath". This graphic was inspired by a figure in reference [10].

The Schrödinger equation, the Heisenberg equation and the von Neumann equation are used to describe the time evolution of a system in fundamental quantum physics.

This reaches its limit if relativistic effects come into play. For most systems these equations cannot be solved analytically. The description of a closed system, i.e. a system that is completely isolated from its environment, is always an approximation since it's not possible to realise this condition in an experiment. To rigorously describe the dynamics of a real system therefore all particles from the environment and interactions with the surroundings have to be taken into account. Solving these equations even numerically can be very challenging. The idea of open systems is to simplify the description by conceptionally separating a system from it's environment. This idea is depicted in figure 3.1. Unlike closed systems these systems interact with their environment. In our case the system consists of the quantum dot as a three level system interacting with a laser. The environment induces dissipative effects to the system.

Instead of pure states, the more general formalism of density matrices is used to describe the state of a system within this context. The dynamics of open systems is given by solving the master equation which corresponds to the von Neumann equation for closed systems. The following lines of discussion and notation are strongly influenced by reference [10]. We use the master equation in Lindblad form:

$$\dot{\rho} = -\frac{i}{\hbar}[H, \rho] + \sum_j (R_j \rho R_j^\dagger - \frac{1}{2} R_j^\dagger R_j \rho - \frac{1}{2} \rho R_j^\dagger R_j), \tag{3.1}$$

where H and ρ are the Hamiltonian and the density matrix of the system. R_js are called jump operators and correspond to the dissipation induced by the environment (see section 3.3 for the discussion of dissipative effects). The first part of the equation corresponds to the unitary time evolution of the system. The second part accounts for the effect of the bath. Equation 3.1 describes a Markovian time evolution. That means that the time evolution of ρ only depends on its present state and can be written as $\dot{\rho} = L\rho$ with the linear operator L which is sometimes called "Liouvillian".

3.2 System Hamiltonian

This section offers a derivation of the Hamiltonian for the quantum dot which is interacting with a laser. The starting point is the Hamiltonian for a three level system interacting with monochromatic classical light within the dipole representation:

$$\hat{H} = \underbrace{E_g|\mathrm{g}\rangle\langle\mathrm{g}| + E_x|\mathrm{x}\rangle\langle\mathrm{x}| + E_b|\mathrm{b}\rangle\langle\mathrm{b}|}_{\hat{H}_0} \underbrace{-\hat{\vec{d}}\vec{E}_{\mathrm{cl}}(t)}_{\hat{H}_{\mathrm{int}}}. \tag{3.2}$$

The classical electrical field can be written as [11]

$$\vec{E}_{\mathrm{cl}}(t) = E_{\mathrm{L}}(t)\ \vec{\epsilon}\ e^{i\omega_{\mathrm{L}} t} + \text{c.c.}^1 \tag{3.3}$$

with amplitude $E_{\mathrm{L}}(t)$, laser frequency ω_{L} and polarisation vector $\vec{\epsilon}$. The energy levels of the quantum dot can be expressed in terms of the laser frequency and the detuning for the exciton Δ_x and biexciton Δ_b level:

$$E_g := 0,\ E_x := \omega_{\mathrm{L}} + \Delta_x \text{ and } E_b := 2\omega_{\mathrm{L}} - \Delta_b. \tag{3.4}$$

---

[1] The expression of the field does not show any spatial dependence. The long-wavelength approximation is assumed. The laser pulse will later be approximated by a Gaussian, which can be written in $E_{\mathrm{L}}(t)$.

The ground state energy is set to 0 and $\hbar$ is set to 1 here. $\hat{H}_{\text{int}}$ can be simplified using the following:

1. The diagonal matrix elements of $\hat{\vec{d}}$ vanish, i.e. $\langle \text{g}|\hat{\vec{d}}|\text{g}\rangle =: \vec{d}_{gg} = 0 = \vec{d}_{xx} = \vec{d}_{bb}$.
2. Assume that the Rabi frequencies
$$\Omega_{ij}(t) := -\vec{d}_{ij}\ \vec{\epsilon}\ E_{\text{L}}(t) \tag{3.5}$$
are real, i.e. $\Omega_{ij} = \Omega_{ij}^{*}$, for all $i, j \in \{g, x, b\}$.
3. $\Omega_{ij} = \Omega_{ji}$ for all $i, j \in \{g, x, b\}$.
4. The ground and biexciton state do not couple directly, i.e. $\Omega_{gb} = 0 = \Omega_{bg}$.
5. Assume that the ground state-exciton coupling has the same strength as the exciton-biexciton coupling, i.e.
$$\Omega := \Omega_{gx} = \Omega_{xb}. \tag{3.6}$$

Therefore

$$\begin{aligned} \hat{H}_{int} = -\hat{\vec{d}}\vec{E}_{\text{cl}}(t) &= -\underbrace{(|\text{g}\rangle\langle\text{g}| + |\text{x}\rangle\langle\text{x}| + |\text{b}\rangle\langle\text{b}|)}_{\mathbb{1}}\ \hat{\vec{d}}\ \underbrace{(|\text{g}\rangle\langle\text{g}| + |\text{x}\rangle\langle\text{x}| + |\text{b}\rangle\langle\text{b}|)}_{\mathbb{1}}\ \vec{E}_{\text{cl}}(t) \\ &= \Omega(t)\ (e^{i\omega_{\text{L}}t} + e^{-i\omega_{\text{L}}t})(|\text{g}\rangle\langle\text{x}| + |\text{x}\rangle\langle\text{b}| + \text{h.c.}). \end{aligned} \tag{3.7}$$

A unitary transformation helps to perform the rotating wave approximation and thus to get an easier expression. Here the transformation $\hat{U} := e^{i(\omega_{\text{L}}+\Delta_b)t|\text{x}\rangle\langle\text{x}|}e^{i(2\omega_{\text{L}}+\Delta_b)t|\text{b}\rangle\langle\text{b}|}$ will be used:

$$\begin{aligned} \tilde{\hat{H}} &:= \hat{U}\hat{H}\hat{U}^{\dagger} + i(\partial_t\hat{U})\hat{U}^{\dagger} \\ &= (\Delta_x - \Delta_b)|\text{x}\rangle\langle\text{x}| - 2\Delta_b|\text{b}\rangle\langle\text{b}| + \Omega(t)[(1 + e^{-i2\omega_{\text{L}}t})(e^{-i\Delta_b t}|\text{g}\rangle\langle\text{x}| + |\text{x}\rangle\langle\text{b}|) + h.c.]. \end{aligned} \tag{3.8}$$

Performing the rotating wave approximation here means dropping the terms that contain the double laser frequency, i.e. the term with the factor $e^{-2i\omega_{\text{L}}t}$ and its complex conjugate. With this, the Hamiltonian (omitting the tilde) reads

$$\boxed{\hat{H}(t) = (\Delta_x - \Delta_b)|\text{x}\rangle\langle\text{x}| - 2\Delta_b|\text{b}\rangle\langle\text{b}| + \Omega(t)[(e^{-i\Delta_b t}|\text{g}\rangle\langle\text{x}| + |\text{x}\rangle\langle\text{b}|) + \text{h.c.}]}. \tag{3.9}$$

Compared to the Hamiltonian in the project's latest publication [1], we find an additional oscillating factor $e^{-i\Delta_b t}$ in the interaction part. However, the Hamiltonians coincide for a resonant excitation, i.e. $\Delta_b = 0$. It is also possible to further transform the Hamiltonian to a form without the oscillating factor using the unitary $\hat{U} := e^{i\Delta_b t}|\text{g}\rangle\langle\text{g}| + |\text{x}\rangle\langle\text{x}| + |\text{b}\rangle\langle\text{b}|$. This leads to the additional diagonal term $-\Delta_b|\text{g}\rangle\langle\text{g}|$:

$$\begin{aligned} \tilde{\hat{H}} &= \hat{U}\hat{H}\hat{U}^{\dagger} + i(\partial_t\hat{U})\hat{U}^{\dagger} \\ &= -\Delta_b|\text{g}\rangle\langle\text{g}| + (\Delta_x - \Delta_b)|\text{x}\rangle\langle\text{x}| - 2\Delta_b|\text{b}\rangle\langle\text{b}| + \Omega(t)[(|\text{g}\rangle\langle\text{x}| + |\text{x}\rangle\langle\text{b}|) + h.c.]. \end{aligned} \tag{3.10}$$

3.3 Dissipation

Within our model we consider four different dissipative effects: the decay of the biexciton to the exciton and the decay of the exciton to the ground state. Additionally, we include dephasing between the biexciton state and the exciton state, as well as between the exciton state and the ground state. We assign a Lindblad operator to all of these processes [1]:

$$\begin{aligned}
&\text{Decay:}\\
&R_1 = \sqrt{\gamma_b}\ |\mathrm{x}\rangle\langle\mathrm{b}| \text{ with } \gamma_b = 1/771 \text{ THz},\\
&R_2 = \sqrt{\gamma_x}\ |\mathrm{g}\rangle\langle\mathrm{x}| \text{ with } \gamma_x = 1/405 \text{ THz}.\\
&\text{Dephasing:}\\
&R_3 = \sqrt{\gamma_{bx}}\ (|\mathrm{b}\rangle\langle\mathrm{b}| - |\mathrm{x}\rangle\langle\mathrm{x}|) \text{ with } \gamma_{bx} = \gamma_{I_0}^{bx}(\tfrac{\Omega(t)}{\Omega_d})^n,\\
&R_4 = \sqrt{\gamma_{xg}}\ (|\mathrm{x}\rangle\langle\mathrm{x}| - |\mathrm{g}\rangle\langle\mathrm{g}|) \text{ with } \gamma_{xg} = \gamma_{I_0}^{xg}(\tfrac{\Omega(t)}{\Omega_d})^n.
\end{aligned} \tag{3.11}$$

The values of γ_b and γ_x are determined by experimental data [1, Supplemental Material].

The dephasing rates nonlinearly depend on the laser's intensity, while per definition these rates depend on powers of the Rabi frequency $\Omega(t)$. The Rabi frequency however can be related to the laser intensity. This can be reasoned as follows:

We approximate the pulsed laser to have a Gaussian profile. The form of the Rabi frequency is modeled by [1]

$$\Omega(t) = \Omega_0 \exp\left(-\frac{\ln(2)(t-t_0)^2}{\sigma^2}\right). \tag{3.12}$$

The intensity of a Gaussian beam is proportional to the square of the absolute value of the electric field [12]:

$$I \propto |E|^2. \tag{3.13}$$

The expression for the electric field which is generated by the laser is given in equation 3.3. Note that the spatial profile of this field is not discussed within this work since the quantum dot is approximated to have no spatial extension which is important for the long-wavelength approximation. Therefore we only consider the field's time dependency here. The Rabi frequency was defined as

$$\Omega_{ij}(t) = -\vec{d}_{ij}\ \vec{\epsilon}\ E_L(t).$$

If the dipole operator and the polarisation vector are constant, this leads to

$$\Omega(t) \propto E_{\mathrm{L}}(t). \tag{3.14}$$

If E_{L} is real and if the polarisation vector is real and normalised, the absolute value of the electric field is given by

$$|E_{\mathrm{cl}}(t)| = E_{\mathrm{L}}(t)(2 + 2\cos(2\omega_{\mathrm{L}}t)). \tag{3.15}$$

By using equation 3.13 we find

$$\sqrt{I} \propto \Omega(t)(2 + 2\cos(2\omega_{\mathrm{L}}t)). \tag{3.16}$$

This relates the intensity to the Rabi frequency.
Ω_d, which appears in the expression of the dephasing rates, is necessary to obtain the correct units and it's value is 1 THz. The dephasing amplitudes are determined by processing experimental data: $\gamma_{I_0}^{bx} = 0.0219$ THz and $\gamma_{I_0}^{xg} = 0.0349$ THz [1]. The exponent n indicates to which power the dephasing rate depends on the laser intensity. The values $n = 2$ (linear dependency) and $n = 4$ (quadratic dependency) were both in accordance with results from the measurement [1].

Chapter 4

Tomography

The aim of the experiment that is discussed throughout this thesis is to create time-bin entangled photons. The post-selected, reconstructed state of these photons is then compared to a maximally entangled state by calculating the fidelity. It is therefore necessary to be able to reconstruct a quantum state for the created photons. Within this chapter we want to describe the tomographic method that is used to reconstruct the state. This will be followed by a discussion on the experimental realization of the tomographic scheme. We will conclude this chapter by a presentation of how the state of the photons could be reconstructed theoretically from simulating the photon counts.

The basic tomographic method that has been adopted for the experiment was described by James et al. [5]. Takesue and Noguchi [6] have proposed the implementation of this method for time-bin entangled photons. For the discussion of tomography we will follow ideas and calculations presented in these publications.

4.1 Tomographic Method

The tomographic method is based on projective (post selective) measurements of the photons that are emitted by the quantum dot. For this purpose we define a set of 16 states $\{|\psi_i\rangle\}_{i=1}^{16}$ with the two-photon states

$$|\psi_i\rangle := |\phi_{1_i}\rangle|\phi_{2_i}\rangle \text{ where } |\phi_{1_i}\rangle, |\phi_{2_i}\rangle \in \{|\mathrm{e}\rangle, |\mathrm{l}\rangle, |+\rangle, |\mathrm{R}\rangle\}. \tag{4.1}$$

Here the one-photon states $|\mathrm{e}\rangle$ ($|\mathrm{l}\rangle$) correspond to an early (late) emission of the photon. They form a basis in the two-dimensional Hilbert space to describe time-bin encoding for a single photon. The other two states are a superposition of those: $|+\rangle = \frac{1}{\sqrt{2}}(|\mathrm{e}\rangle + |\mathrm{l}\rangle)$ and $|\mathrm{R}\rangle = \frac{1}{\sqrt{2}}(|\mathrm{e}\rangle - i|\mathrm{l}\rangle)$.

The two-photon density matrix ρ is projected onto the states $\{|\psi_i\rangle\}_{i=1}^{16}$. Portions of photonic states with less or more then two photons are not captured by this method. In this sense we perform a post-selection by truncating the states of less or more then two photons and projecting the photons solely on two-photon states. With the use of photon detectors we focus on how many counts n_ν we obtain by multiple projections onto the state $|\psi_\nu\rangle$ for all ν. Since both photons are measured individually, this is realized via coincidence-counts. The number of counts is given by

$$n_\nu = c\langle\psi_\nu|\rho|\psi_\nu\rangle \text{ for all } \nu, \tag{4.2}$$

where c is a constant efficiency factor that depends on the experimental realization. A relation to determine c can be found below.
The set $\{n_\nu\}_{\nu=1}^{16}$ are the measurement outcomes of our experiment. To reconstruct the density matrix ρ from these values one needs a mathematical relation between ρ and $\{n_\nu\}_{\nu=1}^{16}$. Let's begin the derivation for this expression by decomposing the density matrix:

$$\underline{\underline{\rho}} = \sum_{i=1}^{16} \underline{\underline{\Gamma_i}} r_i = \vec{\underline{\underline{\Gamma}}} \vec{r} \tag{4.3}$$

with $\underline{\underline{\Gamma_i}} := \underline{\underline{\sigma_{1_i}}} \otimes \underline{\underline{\sigma_{2_i}}}$ where $1_i, 2_i \in \{0,1,2,3\}$. The matrices $\underline{\underline{\sigma_{1_i}}}, \underline{\underline{\sigma_{2_i}}}$ are defined by $\underline{\underline{\sigma_0}} := \underline{\underline{\mathbb{1}_2}}$, $\underline{\underline{\sigma_1}} := \underline{\underline{\sigma_x}}$, $\underline{\underline{\sigma_2}} := \underline{\underline{\sigma_y}}$ and $\underline{\underline{\sigma_3}} := \underline{\underline{\sigma_z}}$ with $\underline{\underline{\sigma_x}}, \underline{\underline{\sigma_y}}, \underline{\underline{\sigma_z}}$ being the three Pauli matrices.
For this calculation matrices are underlined twice such that it is more convenient to distinguish them from numbers. The definition of $\underline{\underline{\Gamma_i}} := \underline{\underline{\sigma_{1_i}}} \otimes \underline{\underline{\sigma_{2_i}}}$ for all $i \in [1,16]$ should be chosen such that all possible combinations of the $\underline{\underline{\sigma_j}}$ matrices are contained within the sum of equation 4.3. The chosen order of combinations however is not important as long as it is kept consistent throughout the calculation. The vector $\vec{r}$ contains the coefficients for this decomposition. To reconstruct the density matrix, these coefficients will be related to the vector

$$\vec{n} := \begin{pmatrix} n_1 \\ n_2 \\ \vdots \\ n_{16} \end{pmatrix} \tag{4.4}$$

which contains the measurement outcomes. Inserting equation 4.3 into 4.2 gives

$$n_\nu = c \sum_{i=1}^{16} \underbrace{\langle \psi_\nu | \underline{\underline{\Gamma_i}} | \psi_\nu \rangle}_{=:B_{\nu,i}} r_i. \tag{4.5}$$

Here the c-numbers $B_{\nu,i}$ are defined. They can be written as a matrix:

$$\underline{\underline{B}} := \begin{pmatrix} B_{1,1} & \cdots & B_{1,16} \\ \vdots & & \vdots \\ B_{16,1} & \cdots & B_{16,16} \end{pmatrix}. \tag{4.6}$$

With this definition equation 4.5 can be written as

$$\vec{n} = c\underline{\underline{B}}\vec{r}. \tag{4.7}$$

Note that $\{\underline{\underline{\Gamma_i}}\}_{i=1}^{16}$, $\{|\psi_i\rangle\}_{i=1}^{16}$ and $\underline{\underline{B}}$ are static mathematical objects that are independent from the measurement outcome and furthermore do not depend on any variable. Equation 4.7 relates the measurement outcomes $\vec{n}$ to the decomposition coefficients $\vec{r}$. This can be written as

$$\vec{r} = \frac{1}{c}\underline{\underline{B}}^{-1}\vec{n}, \tag{4.8}$$

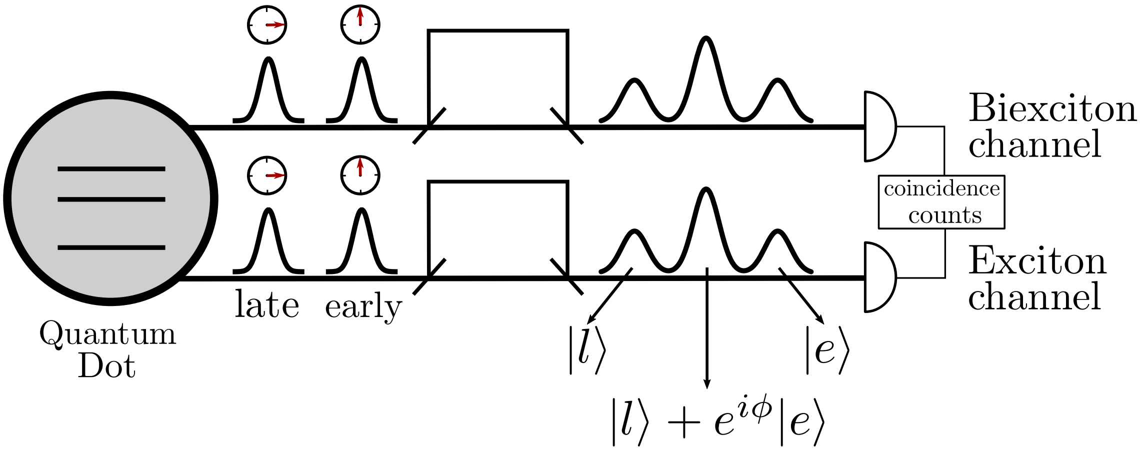

Figure 4.1: Scheme of the experimental realization of the tomographic method. Parts of this figure can be found in similar form in reference [6]. This figure is an extension of the right hand side of figure 2.2.

with $\underline{\underline{B}}^{-1}$ being the inverse matrix of $\underline{\underline{B}}$. Inserting this relation into the decomposition 4.3 gives

$$\begin{aligned}\rho &= \frac{1}{c}\vec{\underline{\underline{\Gamma}}}\,\underline{\underline{B}}^{-1}\vec{n} = \frac{1}{c}\sum_{i=1}^{16}\underline{\underline{\Gamma_i}}\underbrace{(\underline{\underline{B}}^{-1}\vec{n})_i}_{=\sum_{k=1}^{16}B^{-1}_{i,k}n_k} \\ &= \frac{1}{c}\sum_{i,k}\underline{\underline{\Gamma_i}}B^{-1}_{i,k}n_k.\end{aligned} \tag{4.9}$$

With the definition $\underline{\underline{M_k}} := \sum_{i=1}^{16}\underline{\underline{\Gamma_i}}B^{-1}_{i,k}$ this equation reads

$$\boxed{\rho = \frac{1}{c}\sum_{k=1}^{16}\underline{\underline{M_k}}n_k}. \tag{4.10}$$

To obtain an expression for c one may take the trace on both sides:

$$\begin{aligned}\mathrm{tr}(\rho) = 1 &= \frac{1}{c}\sum_{k=1}^{16}\mathrm{tr}(\underline{\underline{M_k}})n_k \\ \Rightarrow c &= \sum_{k=1}^{16}\mathrm{tr}(\underline{\underline{M_k}})n_k.\end{aligned} \tag{4.11}$$

If the measurement outcomes, i.e. the number of counts, are known, the right hand side of equation 4.10 is known. Therefore, by using this equation, ρ can be reconstructed from the two-photon-counts.

4.2 Experimental Realization

Equation 4.10 relates the density matrix to the number of counts of 16 projective measurements. Within this subsection we present how the projective measurements were realized in the experiment.
As it was explained in chapter 2, two correlated pulses hit the quantum dot. This

eventually leads to the emission of photons that are correlated in their time-bins (see figure 2.2). In general, a single laser pulse may lead to no, one or multiple emitted photon pairs, depending on how many times the biexciton and exciton level are excited and decay. The excitation probability of the quantum dot can be varied by tuning the laser's intensity and the pulse length. Consequently, this changes the energy per pulse. In reference [1], the excitation possibility is given to be 6% for the late pulse, as well as for the early pulse. In figure 4.1, the output of the quantum dot is depicted as pulses and the photon number is not considered. The theoretical discussion of the measurements deals with the electric field emitted by the quantum dot (see section 4.3). The number of emitted photons isn't explicitly considered here either. However, values that are proportional to the number of simulated coincidence counts are discussed in this work. These values are correlated to the number of emitted photons.

Figure 4.1 gives an overview of the measurement procedure: The quantum dot emits light at two distinct emission time spans. Pulses can be assigned to this emission which again are denoted by “early" and “late". This light originates from the biexciton, exciton decay cascade. The biexciton and exciton photons can be distinguished by their wavelength (with a difference of $\Delta\lambda = 1.8$ nm in reference [1]) and are analysed in different channels. Both channels contain an analysis interferometer (which is realized in one bulk interferometer as it is mentioned in subsection 2.3). The output of the interferometers can be split into three peaks:

1. The first peak can be assigned to the early pulse propagating through the short arm of the interferometer. Detecting photons at a time corresponding to this peak can be interpreted as a projective measurement on the state $|\mathrm{e}\rangle$, since this signal can be attributed to the early pulse.

2. The middle peak is a superposition of the early pulse passing through the long arm and the late pulse taking the short arm of the interferometer. By controlling the relative phase between these constituents a corresponding photon detection can be related to a projective measurement on $|+\rangle$ (for $\phi = 0$) and $|\mathrm{R}\rangle$ (for $\phi = \frac{\pi}{2}$). The phase ϕ is introduced in subsection 4.3.1.

3. The last peak can be assigned to the late pulse passing through the long arm of the interferometer. A corresponding photon detection can be interpreted as a projective measurement on $|\mathrm{l}\rangle$.

In this way it is possible to realize the projective measurements on the states $\{|\mathrm{e}\rangle, |\mathrm{l}\rangle, |+\rangle, |\mathrm{R}\rangle\}$ for the biexciton and exciton photons separately. To conduct projective measurements on the two-photon product states $\{|\psi_i\rangle\}_{i=1}^{16}$ from section 4.1, the individual detections have to be performed as coincidence measurements.

In this way, the counts $\{n_i\}_{i=1}^{16}$ can be determined experimentally and the density matrix can be reconstructed using equation 4.10.

4.3 Theoretical Realization

The major aim of this master thesis is to establish a simulation that allows to estimate the reconstructed density matrices of the photons emitted by the quantum dot. This gives a theoretical prediction of experimental results. The simulation is

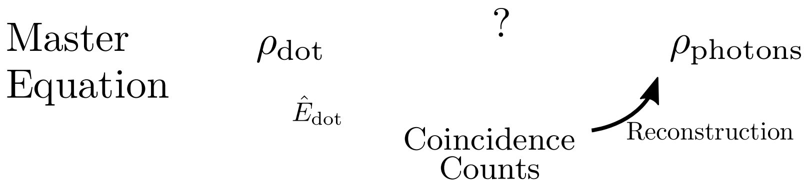

Figure 4.2: Strategy to simulate the photons' density matrix.

based on the quantum optical model introduced in reference [1]. Figure 4.2 gives an overview of the chosen procedure for obtaining the photons' density matrix starting from the master equation given in equation 3.1. Solving the master equation numerically gives the quantum dot's density matrix

$$\rho_{\text{dot}}(t) = \begin{pmatrix} \rho_{gg} & \rho_{gx} & \rho_{gb} \\ \rho_{xg} & \rho_{xx} & \rho_{xb} \\ \rho_{bg} & \rho_{bx} & \rho_{bb} \end{pmatrix} \tag{4.12}$$

for a chosen time interval at discrete time steps. The time arguments of the entries of the quantum dot's density matrix are not written down throughout this work. Nevertheless, they depend on time.

The task is to relate the dot's density matrix to the one of the photon pairs

$$\rho_{\text{photons}} = \begin{pmatrix} \rho_{ee,ee} & \rho_{ee,el} & \rho_{ee,le} & \rho_{ee,ll} \\ \rho_{el,ee} & \rho_{el,el} & \rho_{el,le} & \rho_{el,ll} \\ \rho_{le,ee} & \rho_{le,el} & \rho_{le,le} & \rho_{le,ll} \\ \rho_{ll,ee} & \rho_{ll,el} & \rho_{ll,le} & \rho_{ll,ll} \end{pmatrix}. \tag{4.13}$$

$\rho_{\text{dot}}(t)$ is written in the $\{|\text{g}\rangle, |\text{x}\rangle, |\text{b}\rangle\}$ basis while ρ_{photons} is written in the two-photon basis $\{|\text{ee}\rangle, |\text{el}\rangle, |\text{le}\rangle, |\text{ll}\rangle\}$.

To relate those density matrices $\rho_{\text{dot}}(t) \to \rho_{\text{photons}}$ we undergo a procedure that simulates the experimental measurements. This strategy can be divided into three steps:

1. Find expressions for the electric field operators that correspond to the peaks which make up the output of the analysis interferometer to simulate the experimental measurement setup. This setup is described in section 4.2 and is sketched in figure 4.1.
2. Calculate the number of coincidence counts, given the expressions for the electric field at the detectors.
3. Use the calculated number of coincidence counts to reconstruct the photons' density matrix by utilizing the method introduced in section 4.1.

The first two steps are described in more detail within the following subsections.

4.3.1 Electric field emitted by the quantum dot

The emitted field of a two-level quantum emitter is proportional to the atomic operators $\hat{\sigma}^-, \hat{\sigma}^+$ at retarded time and geometrical factors $\vec{e}(\vec{r})$ and $\vec{e}(\vec{r})^*$ [1, Supplemental Material]:

$$\hat{\vec{E}}(\vec{r},t) = \hat{\vec{E}}^+(\vec{r},t) + \hat{\vec{E}}^-(\vec{r},t) \propto \vec{e}(\vec{r})\hat{\sigma}^-(t - \tfrac{r}{c}) + \vec{e}(\vec{r})^*\hat{\sigma}^+(t - \tfrac{r}{c}). \tag{4.14}$$

The emitted signal has to travel for a time of $\frac{r}{c}$ to reach the position $\vec{r}$. This is indicated by the additional term in the argument of the operators. In the end we are interested in the field emitted by the quantum dot at the position $\vec{r}$ of the detectors. We assume $\vec{r}$ to be constant which leads to a simplified expression:

$$\hat{\vec{E}}(t) \propto \hat{\sigma}^-(t - \tfrac{r}{c}) + \hat{\sigma}^+(t - \tfrac{r}{c}). \tag{4.15}$$

The quantum dot can be interpreted as a set of two cascaded two-level quantum emitters that correspond to the biexciton-exciton and to the exciton-ground state transition.

The expression for the electric field emitted by the quantum dot is structured with respect to the three peaks that can be observed as the output of the analysis interferometers (see figure 4.1):

1. First peak (early pulse transmitted through the short arm):

$$_1\hat{E}^+_{x,b}(t) \propto \hat{\sigma}^-_{x,b}(t). \tag{4.16}$$

2. Middle peak (a superposition of early and late pulse):

$$_2\hat{E}^+_{x,b}(t) \propto \frac{1}{\sqrt{2}}(\hat{\sigma}^-_{x,b}(t+\tau) + e^{i\phi_{x,b}}\ \hat{\sigma}^-_{x,b}(t)). \tag{4.17}$$

3. Third peak (late pulse transmitted through the long arm):

$$_3\hat{E}^+_{x,b}(t) \propto \hat{\sigma}^-_{x,b}(t+\tau). \tag{4.18}$$

The subscript x and b correspond to the exciton and biexciton channel. τ accounts for the time between the early and late pulse. $\phi_{x,b}$ corresponds to the phase shift induced by the analysis interferometer. The term $\frac{r}{c}$ has been dropped in the argument of the $\hat{\sigma}^-_{x,b}$ operator.

The factor $\frac{1}{\sqrt{2}}$ in the expression for $_2\hat{E}^+_{x,b}(t)$ is introduced here for the calculation of the expressions that are proportional to $f_\nu(t)$ in subsection 4.3.2. These expressions are used to estimate the number of coincidence counts.

In the Schrödinger picture, the operators $\hat{\sigma}^-_{x,b}$ and $\hat{\sigma}^+_{x,b}$ are defined by

$$\hat{\sigma}^-_b = |\mathrm{x}\rangle\langle\mathrm{b}|, \hat{\sigma}^-_x = |\mathrm{g}\rangle\langle\mathrm{x}|, \hat{\sigma}^+_b = |\mathrm{b}\rangle\langle\mathrm{x}| \text{ and } \hat{\sigma}^+_x = |\mathrm{x}\rangle\langle\mathrm{g}|. \tag{4.19}$$

Within this work, these operators however will be given in a time-dependent form. There is some freedom in defining the time argument of the operators. The crucial point is that the quantum dot should be evaluated at times when population and coherences build up and decay after the early and late pulse hit the dot. In the equations 4.16 to 4.18, the time argument t corresponds to the early pulse and $t+\tau$ evaluates the dot for the late pulse. Here, t is restricted to an interval: $t \in [0, \tau]$.

The above expressions of the electric field can be used to simulate the number of coincidence counts at the detectors.

4.3.2 Simulated number of coincidence counts

Within the following, an expression that relates the number of coincidence counts to the electric field at the position of the detectors is derived. The number of counts is proportional to the count probability. To derive an expression for the count probability of a single detector exposed to a general quantized electric field $\hat{E}$, consider the probability for a single photon being "lost" due to it's absorption by the detector. This investigation can be extended to the case of a coincidence measurement of two photons. The derivation is based on Daniel Steck's presentation [13, chapter 16.1] of a publication by Roy Glauber [14].
The quantized electric field can be written as

$$\hat{E}(\vec{r},t) = \hat{E}^{+}(\vec{r},t) + \hat{E}^{-}(\vec{r},t) = \sum_j E_j e^{i\vec{k}_j\vec{r}}\ \hat{a}_j(t) + \sum_j E_j e^{-i\vec{k}_j\vec{r}}\ \hat{a}_j^{\dagger}(t). \tag{4.20}$$

E_j is a factor for which the index j indicates the dependency on the field mode frequency ω_j. $\hat{a}_j^{\dagger}$ ($\hat{a}_j$) creates (annihilates) a photon in a mode to which $\vec{k}_j$ can be assigned to. The polarization is not considered here. If a photon is detected, the field's state changes from an initial state $|i\rangle$ to a final state $|f\rangle$. Compared to the initial state, the final state describes the field with a missing photon in a present mode. A probability can be assigned to the detection of a photon at time t:

$$p(t) \propto \lim_{\epsilon\to 0} \sum_f |\langle f|\hat{U}(t+\epsilon, t-\epsilon)|i\rangle|^2. \tag{4.21}$$

Strictly speaking, $p(t)$ is not a probability but a probability distribution since t is a continuous variable. $\hat{U}(t+\epsilon, t-\epsilon)$ is the time evolution operator evaluated for a infinitesimal time interval around t. The sum contains all possible final states. Every summand corresponds to a potential annihilation of the photon that is detected:

$$p(t) \propto \lim_{\epsilon\to 0} \sum_f |\langle f|\hat{U}(t+\epsilon, t-\epsilon)|i\rangle|^2 \propto \sum_f |\langle f|\hat{a}_{j_f}(t)|i\rangle|^2. \tag{4.22}$$

With j_f being an index of the sum in equation 4.20 that corresponds to the mode of the detected photon. Since we deal with proportionalities only, we can insert the annihilation part $\hat{E}^{+}(t)$ of the field. All annihilation operators except one (the one corresponding to the mode of the detected photon) will lead to a vanishing term.

$$\begin{aligned} p(t) \propto \sum_f |\langle f|\hat{E}^{+}(t)|i\rangle|^2 = \sum_f \langle i|\hat{E}^{-}(t)|f\rangle\langle f|\hat{E}^{+}(t)|i\rangle &= \langle i|\hat{E}^{-}(t)\hat{E}^{+}(t)|i\rangle \\ &= \langle \hat{E}^{-}(t)\hat{E}^{+}(t)\rangle \end{aligned} \tag{4.23}$$

For the discussion of a two photon coincidence measurement, consider a detector to be at position $\vec{r}_1$ and another one at $\vec{r}_2$. A field's final state $|f\rangle$ can now be defined in the same fashion as before with two photons being absorbed from the initial state.

$$\begin{aligned} p_{1,2}(t) &\propto \lim_{\epsilon\to 0} \sum_f |\langle f|\hat{U}(t+\epsilon, t-\epsilon)|i\rangle|^2 \propto \sum_f |\langle f|\hat{E}^{+}(\vec{r}_2,t)\hat{E}^{+}(\vec{r}_1,t)|i\rangle|^2 \\ &= \sum_f \langle i|\hat{E}^{-}(\vec{r}_1,t)\hat{E}^{-}(\vec{r}_2,t)|f\rangle\langle f|\hat{E}^{+}(\vec{r}_2,t)\hat{E}^{+}(\vec{r}_1,t)|i\rangle \\ &= \langle \hat{E}^{-}(\vec{r}_1,t)\hat{E}^{-}(\vec{r}_2,t)\hat{E}^{+}(\vec{r}_2,t)\hat{E}^{+}(\vec{r}_1,t)\rangle. \end{aligned} \tag{4.24}$$

With $p_{1,2}(t)$ being the detection probability distribution for a coincidence measurement which is triggered by an absorption at $\vec{r}_1$. The probability distribution is denoted by $p_{2,1}(t)$ if the triggering happened at $\vec{r}_2$.
The probability for a coincidence count within the time interval $[0, t]$ is given by the integral over the probability distribution for a measurement triggered at $\vec{r}_1$ and at $\vec{r}_2$:

$$P(t) = \int_0^t \left(p_{1,2}(t') + p_{2,1}(t')\right)\, \mathrm{d}t'. \tag{4.25}$$

With this it is possible to simulate the number of coincidence counts $\{n_\nu\}_{\nu=1}^{16}$, which correspond to 16 projective measurements onto the states $\{|\psi_\nu\rangle\}_{\nu=1}^{16}$. The number of coincidence counts within the time interval $[0, t]$ is proportional to the corresponding probability:

$$n_\nu(t) \propto P_\nu(t) = \int_0^t \left({}^{\nu}p_{x,b}(t') + {}^{\nu}p_{b,x}(t')\right)\, \mathrm{d}t'. \tag{4.26}$$

ν refers to the states $|\psi_\nu\rangle = |\phi_{1_\nu}\rangle|\phi_{2_\nu}\rangle$ which the photons are projected onto. The subscripts of the probability distribution refer to the detection at the biexciton (b) and exciton (x) channel. Using equation (4.24) we obtain

$$\begin{aligned} &n_\nu(t) \propto \\ &\int_0^t \underbrace{\langle {}_{1_\nu}\hat{E}_x^-(t')\, {}_{2_\nu}\hat{E}_b^-(t')\, {}_{2_\nu}\hat{E}_b^+(t')\, {}_{1_\nu}\hat{E}_x^+(t')\rangle + \langle {}_{2_\nu}\hat{E}_b^-(t')\, {}_{1_\nu}\hat{E}_x^-(t')\, {}_{1_\nu}\hat{E}_x^+(t')\, {}_{2_\nu}\hat{E}_b^+(t')\rangle}_{=:f_\nu(t')}\, \mathrm{d}t' \\ &= \int_0^t f_\nu(t')\, \mathrm{d}t'. \end{aligned} \tag{4.27}$$

The expressions for the electric field have to be chosen according to the state decomposition $|\psi_i\rangle = |\phi_{1_i}\rangle|\phi_{2_i}\rangle$. That means, depending onto which states $|\phi_{1_i}\rangle$ and $|\phi_{2_i}\rangle$ the photons get projected, one has to choose the corresponding expressions for the electric field (equations 4.16 to 4.18) which correspond to the peaks discussed in subsection 4.3.1. $f_\nu(t)$ was introduced to abbreviate the expression.
To simulate the number of coincidence measurements we calculated $f_\nu(t)$ for all of the 16 projective measurements. The results are summarized in table 4.1. An exemplary calculation for some $f_\nu(t)$ is given in the following.

Exemplary calculation of $f_\nu(t)$ for $\nu \in \{1, 2, 5, 6\}$

The definition of $f_\nu(t)$ is given in equation 4.27. Depending on the value of ν, i.e. depending on which state is discussed for the projective measurement, one has to choose the expressions of the electric field accordingly. The three possibilities for $\hat{E}_{x,b}^+(t)$ are given in equations 4.16 to 4.18. The following illustration covers the relations

$$\hat{E}_b^+(t) \propto \frac{1}{\sqrt{2}}\left(\hat{\sigma}_b^-(t+\tau) + e^{i\phi_b}\ \hat{\sigma}_b^-(t)\right) \tag{4.28}$$

and

$$\hat{E}_x^+(t) \propto \frac{1}{\sqrt{2}}\left(\hat{\sigma}_x^-(t+\tau) + e^{i\phi_x}\ \hat{\sigma}_x^-(t)\right). \tag{4.29}$$

These expressions correspond to the middle peak of the interferometer's output. Projective measurements onto a product of single particle states which show a superposition of the late and early pulse can be assigned to detections at this peak.

ν	Biexciton	Exciton	$\lvert\psi_\nu\rangle$	$f_\nu(t)$ (proportional)
1	$\lvert+\rangle$	$\lvert+\rangle$	$\frac{1}{2}(\lvert\text{ee}\rangle+\lvert\text{el}\rangle+\lvert\text{le}\rangle+\lvert\text{ll}\rangle)$	$\frac{1}{2}(\rho_{bb}(1+\rho_{xx})+2\rho_{bx}\rho_{xb}+\rho_{bg}\rho_{gb}+\rho_{xx}\rho_{bb})$
2	$\lvert+\rangle$	$\lvert\text{R}\rangle$	$\frac{1}{2}(\lvert\text{ee}\rangle-i\lvert\text{el}\rangle+\lvert\text{le}\rangle-i\lvert\text{ll}\rangle)$	$\frac{1}{2}(\rho_{bb}(1+\rho_{xx})+2\rho_{bx}\rho_{xb}+\rho_{xx}\rho_{bb})$
3	$\lvert+\rangle$	$\lvert\text{e}\rangle$	$\frac{1}{\sqrt{2}}(\lvert\text{ee}\rangle+\lvert\text{le}\rangle)$	$\frac{1}{2}(\rho_{bb}(1+\rho_{xx})+2\rho_{bx}\rho_{xb}+\rho_{xx}\rho_{bb})$
4	$\lvert+\rangle$	$\lvert\text{l}\rangle$	$\frac{1}{\sqrt{2}}(\lvert\text{el}\rangle+\lvert\text{ll}\rangle)$	$\frac{1}{2}(\rho_{bb}(1+\rho_{xx})+2\rho_{bx}\rho_{xb}+\rho_{xx}\rho_{bb})$
5	$\lvert\text{R}\rangle$	$\lvert+\rangle$	$\frac{1}{2}(\lvert\text{ee}\rangle+\lvert\text{el}\rangle-i\lvert\text{le}\rangle-i\lvert\text{ll}\rangle)$	$\frac{1}{2}(\rho_{bb}(1+\rho_{xx})+\rho_{xx}\rho_{bb})$
6	$\lvert\text{R}\rangle$	$\lvert\text{R}\rangle$	$\frac{1}{2}(\lvert\text{ee}\rangle-i\lvert\text{el}\rangle-i\lvert\text{le}\rangle-\lvert\text{ll}\rangle)$	$\frac{1}{2}(\rho_{bb}(1+\rho_{xx})-\rho_{bg}\rho_{gb}+\rho_{xx}\rho_{bb})$
7	$\lvert\text{R}\rangle$	$\lvert\text{e}\rangle$	$\frac{1}{\sqrt{2}}(\lvert\text{ee}\rangle-i\lvert\text{le}\rangle)$	$\frac{1}{2}(\rho_{bb}(1+\rho_{xx})+\rho_{xx}\rho_{bb})$
8	$\lvert\text{R}\rangle$	$\lvert\text{l}\rangle$	$\frac{1}{\sqrt{2}}(\lvert\text{el}\rangle-i\lvert\text{ll}\rangle)$	$\frac{1}{2}(\rho_{bb}(1+\rho_{xx})+\rho_{xx}\rho_{bb})$
9	$\lvert\text{e}\rangle$	$\lvert+\rangle$	$\frac{1}{\sqrt{2}}(\lvert\text{ee}\rangle+\lvert\text{el}\rangle)$	$\frac{1}{2}(\rho_{bb}(1+\rho_{xx})+\rho_{xx}\rho_{bb})$
10	$\lvert\text{e}\rangle$	$\lvert\text{R}\rangle$	$\frac{1}{\sqrt{2}}(\lvert\text{ee}\rangle-i\lvert\text{el}\rangle)$	$\frac{1}{2}(\rho_{bb}(1+\rho_{xx})+\rho_{xx}\rho_{bb})$
11	$\lvert\text{e}\rangle$	$\lvert\text{e}\rangle$	$\lvert\text{ee}\rangle$	ρ_{bb}
12	$\lvert\text{e}\rangle$	$\lvert\text{l}\rangle$	$\lvert\text{el}\rangle$	$2\rho_{xx}\rho_{bb}$
13	$\lvert\text{l}\rangle$	$\lvert+\rangle$	$\frac{1}{\sqrt{2}}(\lvert\text{le}\rangle+\lvert\text{ll}\rangle)$	$\frac{1}{2}(\rho_{bb}(1+\rho_{xx})+\rho_{xx}\rho_{bb})$
14	$\lvert\text{l}\rangle$	$\lvert\text{R}\rangle$	$\frac{1}{\sqrt{2}}(\lvert\text{le}\rangle-i\lvert\text{ll}\rangle)$	$\frac{1}{2}(\rho_{bb}(1+\rho_{xx})+\rho_{xx}\rho_{bb})$
15	$\lvert\text{l}\rangle$	$\lvert\text{e}\rangle$	$\lvert\text{le}\rangle$	$2\rho_{xx}\rho_{bb}$
16	$\lvert\text{l}\rangle$	$\lvert\text{l}\rangle$	$\lvert\text{ll}\rangle$	ρ_{bb}

Table 4.1: The tomographic method in the form it was introduced in section 4.1 requires a set of 16 projective measurements. To simulate these measurements we calculated $f_\nu(t)$ in order to mimic the number of coincidence counts theoretically. The second and third column indicate to which state the light is projected to in each channel and the subsequent column gives the resulting combined state. The last column summarizes the corresponding expressions of $f_\nu(t)$. These expressions are not equal but proportional to $f_\nu(t)$. The time arguments have not been displayed here even though the elements of the quantum dot's density matrix are time dependent.

In our case, these single particle states are $\lvert+\rangle$ and $\lvert\text{R}\rangle$ and their products are listed in table 4.1 for the rows with $\nu = 1, 2, 5, 6$. In general $f_\nu(t)$ can be written as

$$f_\nu(t) = {}^{\nu}\tilde{p}_{x,b}(t) + {}^{\nu}\tilde{p}_{b,x}(t), \tag{4.30}$$

with

$${}^{\nu}\tilde{p}_{x,b}(t) = \langle {}_{1\nu}\hat{E}_x^-(t')\ {}_{2\nu}\hat{E}_b^-(t')\ {}_{2\nu}\hat{E}_b^+(t')\ {}_{1\nu}\hat{E}_x^+(t')\rangle \tag{4.31}$$

and

$${}^{\nu}\tilde{p}_{b,x}(t) = \langle {}_{2\nu}\hat{E}_b^-(t')\ {}_{1\nu}\hat{E}_x^-(t')\ {}_{1\nu}\hat{E}_x^+(t')\ {}_{2\nu}\hat{E}_b^+(t')\rangle. \tag{4.32}$$

The tilde indicates that these expressions are proportional but not identical to the probability distributions: ${}^{\nu}p_{x,b}(t) \propto {}^{\nu}\tilde{p}_{x,b}(t)$ and ${}^{\nu}p_{b,x}(t) \propto {}^{\nu}\tilde{p}_{b,x}(t)$ (see equation 4.24).

The calculation for ${}^{\nu}\tilde{p}_{b,x}(t)$ and ${}^{\nu}\tilde{p}_{x,b}(t)$ is presented successively in the following with the expressions for the electric field given in equation 4.28 and 4.29.

$$\begin{aligned}\tilde{p}_{b,x}(t) =&\langle \hat{E}_b^-(t)\hat{E}_x^-(t)\hat{E}_x^+(t)\hat{E}_b^+(t)\rangle\\ \overset{\text{eq. 4.28, 4.29}}{\propto}&\tfrac{1}{4}\langle(\hat{\sigma}_b^+(t+\tau)+e^{-i\phi_b}\ \hat{\sigma}_b^+(t))(\hat{\sigma}_x^+(t+\tau)+e^{-i\phi_x}\ \hat{\sigma}_x^+(t))\\ &(\hat{\sigma}_x^-(t+\tau)+e^{i\phi_x}\ \hat{\sigma}_x^-(t))(\hat{\sigma}_b^-(t+\tau)+e^{i\phi_b}\ \hat{\sigma}_b^-(t))\rangle\\ =&\ \tfrac{1}{4}\langle\left.\begin{array}{l}(|\mathrm{b}\rangle\langle\mathrm{x}|(t+\tau)+e^{-i\phi_b}|\mathrm{b}\rangle\langle\mathrm{x}|(t))\\ \quad\left.\begin{array}{l}(|\mathrm{x}\rangle\langle\mathrm{g}|(t+\tau)+e^{-i\phi_x}|\mathrm{x}\rangle\langle\mathrm{g}|(t))\\(|\mathrm{g}\rangle\langle\mathrm{x}|(t+\tau)+e^{i\phi_x}|\mathrm{g}\rangle\langle\mathrm{x}|(t))\end{array}\right\}=:\mathrm{(I)}\end{array}\right\}=:\mathrm{(II)}\\ &\quad(|\mathrm{x}\rangle\langle\mathrm{b}|(t+\tau)+e^{i\phi_b}|\mathrm{x}\rangle\langle\mathrm{b}|(t))\rangle\end{aligned}\tag{4.33}$$

ν is left out within this calculation. Depending on the choice of ϕ_b and ϕ_x, this calculation can correspond to the case $\nu = 1, 2, 5, 6$. The operators have been expressed by their equivalents of the Schrödinger picture though they still depend on time which is indicated by the time argument. However, when combining two of these time dependent operators with the same time argument, they behave exactly like in the Schrödinger picture:

$$\begin{aligned}|\mathrm{n}\rangle\langle\mathrm{m}|(t)\ |\mathrm{k}\rangle\langle\mathrm{l}|(t) = \hat{U}(t)|\mathrm{n}\rangle\langle\mathrm{m}|\hat{U}^\dagger(t)\ \hat{U}(t)|\mathrm{k}\rangle\langle\mathrm{l}|\hat{U}^\dagger(t) &= \hat{U}(t)\delta_{mk}|\mathrm{n}\rangle\langle\mathrm{l}|\hat{U}^\dagger(t)\\ &= \delta_{mk}|\mathrm{n}\rangle\langle\mathrm{l}|(t).\end{aligned}\tag{4.34}$$

To continue with the calculation, an important assumption is made: The quantum dot is initially in the ground state and at the time the second pulse hits the quantum dot, we assume that all of it's excitations by the first pulse have decayed and that all the population is again in the ground state. The quantum dot has completely "forgotten" the first pulse, when the second one arrives. This assumption leads to three simplifications we will make use of:

1. For the quantum dot's density matrix, we assume
$$\rho(t+\tau) = \rho(t) =: \rho. \tag{4.35}$$
2. Operators at time t and $t+\tau$ commute, i.e. $[\hat{O}_1(t), \hat{O}_2(t+\tau)] = 0$.
3. The expectation value of the concatenation of operators at time t and $t+\tau$ factorizes, i.e.
$$\langle\hat{O}_1(t)\hat{O}_2(t+\tau)\rangle = \langle\hat{O}_1(t)\rangle\langle\hat{O}_2(t+\tau)\rangle. \tag{4.36}$$

Here, $\hat{O}_{1,2}$ denote the operators that appear within this calculation, i.e.

$$\hat{O}_{1,2} \in \{\sigma_b^+, \sigma_b^-, \sigma_x^+, \sigma_x^-\}.$$

Within this approach, the variable t should not have values greater then τ, i.e. $t \in [0, \tau]$, since the symmetry in time would be broken otherwise.
Equation 4.33 has been split into parts which will be calculated separately:

$$\mathrm{(I)} = |\mathrm{x}\rangle\langle\mathrm{x}|(t+\tau)+e^{i\phi_x}|\mathrm{x}\rangle\langle\mathrm{g}|(t+\tau)\ |\mathrm{g}\rangle\langle\mathrm{x}|(t)+|\mathrm{x}\rangle\langle\mathrm{x}|(t)+e^{-i\phi_x}|\mathrm{g}\rangle\langle\mathrm{x}|(t+\tau)\ |\mathrm{x}\rangle\langle\mathrm{g}|(t-\tau), \tag{4.37}$$

$$\begin{aligned}(\text{II}) =&(|\text{b}\rangle\langle\text{x}|(t+\tau)+e^{-i\phi_b}|\text{b}\rangle\langle\text{x}|(t))(\text{I})\\ =&|\text{b}\rangle\langle\text{x}|(t+\tau)+e^{i\phi_x}|\text{b}\rangle\langle\text{g}|(t+\tau)\ |\text{g}\rangle\langle\text{x}|(t)+|\text{b}\rangle\langle\text{x}|(t+\tau)|\text{x}\rangle\langle\text{x}|(t)\\ &+e^{-i\phi_b}|\text{x}\rangle\langle\text{x}|(t+\tau)\ |\text{b}\rangle\langle\text{x}|(t)+e^{-i\phi_b}|\text{b}\rangle\langle\text{x}|(t)+e^{-i(\phi_x+\phi_b)}|\text{g}\rangle\langle\text{x}|(t+\tau)\ |\text{b}\rangle\langle\text{g}|(t)\end{aligned}\tag{4.38}$$

and thereby

$$\begin{aligned}\tilde{p}_{b,x}(t) \propto&\tfrac{1}{4}\langle\ (\text{II})(|\text{x}\rangle\langle\text{b}|(t+\tau)+e^{i\phi_b}|\text{x}\rangle\langle\text{b}|(t))\ \rangle\\ =&\ \tfrac{1}{4}\langle\ |\text{b}\rangle\langle\text{b}|(t+\tau)+|\text{b}\rangle\langle\text{b}|(t+\tau)|\text{x}\rangle\langle\text{x}|(t)+e^{-i\phi_b}|\text{x}\rangle\langle\text{b}|(t+\tau)\ |\text{b}\rangle\langle\text{x}|(t)\\ &+e^{-i\phi_b}|\text{x}\rangle\langle\text{b}|(t+\tau)\ |\text{b}\rangle\langle\text{x}|(t)+e^{-i(\phi_x+\phi_b)}|\text{g}\rangle\langle\text{b}|(t+\tau)\ |\text{b}\rangle\langle\text{g}|(t)\\ &+e^{i\phi_b}|\text{b}\rangle\langle\text{x}|(t+\tau)\ |\text{x}\rangle\langle\text{b}|(t)+e^{i(\phi_x+\phi_b)}|\text{b}\rangle\langle\text{g}|(t+\tau)\ |\text{g}\rangle\langle\text{b}|(t)\\ &+e^{i\phi_b}|\text{b}\rangle\langle\text{x}|(t+\tau)\ |\text{x}\rangle\langle\text{b}|(t)+|\text{x}\rangle\langle\text{x}|(t+\tau)\ |\text{b}\rangle\langle\text{b}|(t)+|\text{b}\rangle\langle\text{b}|(t)\ \rangle.\end{aligned}\tag{4.39}$$

To evaluate the expectation value, consider

$$\langle\ |\text{i}\rangle\langle\text{j}|(t)\ \rangle=\text{tr}(|\text{i}\rangle\langle\text{j}|\rho(t))=\sum_{m,k,l}\langle\text{m}|\ |\text{i}\rangle\langle\text{j}|\ \rho_{kl}(t)|\text{k}\rangle\langle\text{l}|\ |\text{m}\rangle=\rho_{ji}(t).\tag{4.40}$$

Here, the transition into the Schrödinger picture has been done and $\rho_{ji}(t)$ represents the coefficients of the density matrix in the Schrödinger picture. Note that the expectation values is evaluated by using the quantum dot's density matrix. Initially however, the expectation value is associated to the field's initial state $|i\rangle$. The transition from the state of the field to the state of the quantum dot is done due to the fact that the electric field is expressed by operators that act on the Hilbert space of the quantum dot (see equations 4.16 to 4.18).

Now, the final expression for $\tilde{p}_{bx}(t)$ can be derived from equation 4.39 by using equation 4.35, 4.36 and 4.40:

$$\boxed{\begin{aligned}\tilde{p}_{b,x}(t) \propto&\tfrac{1}{4}(\rho_{bb}+\rho_{bb}\rho_{xx}+2e^{-i\phi_b}\rho_{bx}\rho_{xb}+2e^{i\phi_b}\rho_{xb}\rho_{bx}\\ &+e^{-i(\phi_x+\phi_b)}\rho_{bg}\rho_{gb}+e^{i(\phi_x+\phi_b)}\rho_{gb}\rho_{bg}+\rho_{xx}\rho_{bb}+\rho_{bb})\\ =&\ \tfrac{1}{2}(\rho_{bb}(1+\rho_{xx})+2cos(\phi_b)\rho_{bx}\rho_{xb}+cos(\phi_x+\phi_b)\rho_{bg}\rho_{gb})\end{aligned}}\tag{4.41}$$

As before, the time arguments haven been left out here even though the quantum dot's density matrix is time dependent.

In the same fashion $\tilde{p}_{x,b}(t)$ can be calculated:

$$\begin{aligned}\tilde{p}_{x,b}(t) =&\langle\hat{E}_x^-(t)\hat{E}_b^-(t)\hat{E}_b^+(t)\hat{E}_x^+(t)\rangle\\ \overset{\text{eq. 4.28, 4.29}}{\propto}&\left.\begin{array}{l}\tfrac{1}{4}\langle((|\text{x}\rangle\langle\text{g}|(t+\tau)+e^{-i\phi_x}|\text{x}\rangle\langle\text{g}|(t))\\ \left.\begin{array}{l}(|\text{b}\rangle\langle\text{x}|(t+\tau)+e^{-i\phi_b}|\text{b}\rangle\langle\text{x}|(t))\\ (|\text{x}\rangle\langle\text{b}|(t+\tau)+e^{i\phi_b}|\text{x}\rangle\langle\text{b}|(t))\end{array}\right\}=:(\text{III})\end{array}\right\}=:(\text{IV})\\ &(|\text{g}\rangle\langle\text{x}|(t+\tau)+e^{i\phi_x}|\text{g}\rangle\langle\text{x}|(t))\rangle,\end{aligned}\tag{4.42}$$

$$(\text{III})=|\text{b}\rangle\langle\text{b}|(t+\tau)+e^{i\phi_b}|\text{b}\rangle\langle\text{x}|(t+\tau)\ |\text{x}\rangle\langle\text{b}|(t)+e^{-i\phi_b}|\text{x}\rangle\langle\text{b}|(t+\tau)\ |\text{b}\rangle\langle\text{x}|(t)+|\text{b}\rangle\langle\text{b}|(t),\tag{4.43}$$

$$\begin{aligned}(\text{IV})&=(|\text{x}\rangle\langle\text{g}|(t+\tau)+e^{-i\phi_x}|\text{x}\rangle\langle\text{g}|(t))(\text{III})\\ &=|\text{x}\rangle\langle\text{g}|(t+\tau)|\text{b}\rangle\langle\text{b}|(t)+e^{-i\phi_x}|\text{b}\rangle\langle\text{b}|(t+\tau)|\text{x}\rangle\langle\text{g}|(t),\end{aligned}\tag{4.44}$$

$$\begin{aligned}\tilde{p}_{x,b}(t) \propto & \tfrac{1}{4}\langle(\mathrm{IV})(|\mathrm{g}\rangle\langle\mathrm{x}|(t+\tau)+e^{i\phi_x}|\mathrm{g}\rangle\langle\mathrm{x}|(t))\rangle \\ &= \tfrac{1}{4}\langle|\mathrm{x}\rangle\langle\mathrm{x}|(t+\tau)|\mathrm{b}\rangle\langle\mathrm{b}|(t)+|\mathrm{b}\rangle\langle\mathrm{b}|(t+\tau)|\mathrm{x}\rangle\langle\mathrm{x}|(t)\rangle,\end{aligned} \tag{4.45}$$

and finally

$$\boxed{\tilde{p}_{x,b}(t) \propto \tfrac{1}{2}\rho_{xx}\rho_{bb}}. \tag{4.46}$$

This exemplary calculation can now be concluded with the final expression for $f_\nu(t)$:

$$\boxed{\begin{aligned}f_\nu(t) &= {}^\nu\tilde{p}_{x,b}(t) + {}^\nu\tilde{p}_{b,x}(t) \\ &\propto \tfrac{1}{2}(\rho_{bb}(1+\rho_{xx}) + 2\cos(\phi_b)\rho_{bx}\rho_{xb} + \cos(\phi_x+\phi_b)\rho_{bg}\rho_{gb} + \rho_{xx}\rho_{bb})\end{aligned}}. \tag{4.47}$$

This concludes the derivation of the expression for $f_\nu(t)$ with $\nu \in \{1,2,5,6\}$. Expressions for other values of ν are summarized in table 4.1. The derivations for these cases are not explicitly given here, however they follow the same procedure as shown in the exemplary calculation. All expressions for $f_\nu(t)$ depend on the density matrix of the quantum dot. The master equation (see equation 3.1) is solved numerically in order to obtain values for the density matrix elements. These values can be plugged into the expressions for $f_\nu(t)$ and numerically integrated over some time interval. This finally leads to the simulated number of coincidence counts $\{n_\nu\}_{\nu=1}^{16}$ (see equation 4.27).
ρ_{photons} can finally be calculated by plugging the numerical values for $\{n_\nu\}_{\nu=1}^{16}$ in the reconstruction scheme described in section 4.1.

Chapter 5

Results

This thesis focuses on the theoretical prediction and analysis of the density matrix of (post selected) photons emitted by the quantum dot. As stated before, this simulation involves numerically solving the master equation (see equation 3.1) on the basis of the quantum optical model discussed in chapter 3. The Hamiltonian given in reference [1] is used here, which lacks an oscillating factor compared to the one given in equation 3.9. This procedure leads to numerical values for $\rho_{\text{dot}}(t)$, which can be used to reconstruct ρ_{photons} by applying the tomographic method described in chapter 4. A set of the system parameters is given in table 5.1. They play a crucial role in the simulation and analysis. Numerical solutions of $\rho_{\text{dot}}(t)$ are presented in section 5.1. Section 5.2 consists of a presentation of the reconstructed density matrix of the photons ρ_{photons}. In the subsequent section, ρ_{photons} and the number of counts are analysed.

Parameter	Symbol	Value [1]
Detuning between the exciton level and the laser	Δ_x	$2\pi \cdot 0.335$ THz
Detuning between the biexciton level and the energy corresponding to the double laser frequency	Δ_b	0 THz (resonant excitation is assumed)
Measure for the width of the Rabi frequency (see equation 3.12)	σ	variable
Amplitude of the Rabi frequency	Ω_0	variable
Biexciton decay rate	γ_b	1/771 THz
Exciton decay rate	γ_x	1/405 THz
Biexciton-exciton dephasing rate amplitude	$\gamma_{I_0}^{bx}$	0.0219 THz
Exciton-ground state dephasing rate amplitude	$\gamma_{I_0}^{xg}$	0.0349 THz
Exponent in expression of dephasing rate	n	2 (“linear dephasing"), 4 (“quadratic dephasing")

Table 5.1: Summary of system parameters that are used within the simulation.

We associate σ, a measure for the width of the Rabi frequency, to the laser pulse length and Ω_0, the amplitude of the Rabi frequency, to the amplitude of the laser intensity. The parameters σ and Ω_0 are varied within the following discussion. In

this way, the influence of the laser's settings on the result of the simulation can be studied.
The value of Δ_x in table 5.1 is taken from the supplementary material of the project's latest publication [1]. However, it is possible to derive a different value for Δ_x based on parameters that are given in that publication. The laser frequency is said to be $\lambda_L = 918.7$ nm. The spectral difference between the biexciton and exciton photon is given to be 1.8 nm. We assume a resonant excitation of the biexciton level via the two-photon absorption. That leads to the laser frequency corresponding to the half of the biexciton-groundstate energy difference. Therefore, the difference between the exciton and laser wavelength $\lambda_L - \lambda_x$ can be understood to be 1.8 nm as well. Following these lines of argumentation leads to a different value of Δ_x which approximately differs by the factor of 2 from the value given in table 5.1:

$$\begin{aligned}&\Delta f = \frac{c}{\lambda_x} - \frac{c}{\lambda_L} = c\frac{\lambda_L - \lambda_x}{\lambda_L \cdot \lambda_x} = c(\frac{1.8\text{ nm}}{918.7\text{ nm} \cdot (918.7 + 1.8)\text{ nm}}) \approx 0.638\text{ THz} \\ &\Rightarrow \Delta_x = 2\pi\Delta f \approx 2\pi \cdot 0.638\text{ THz}.\end{aligned} \tag{5.1}$$

The difference in the fidelity of the photons' density matrix due to the different value of Δ_x will be discussed in section 5.3. If not noted otherwise, Δ_x is set to the value given in table 5.1.
For the calculation of the system's dynamics, for the creation of the matrix histograms in this chapter and for parallelization we use QuTiP, a Python toolbox for the numerics in a quantum physical context [15]. The plots presented in this chapter have been created with Matplotlib [16]. Symbolic calculations in the context of the tomographic reconstruction have been done with SymPy [17].

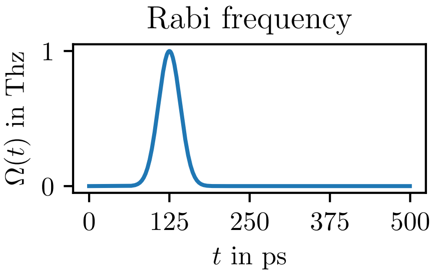

Figure 5.1: Exemplary plot of the Rabi frequency $\Omega(t)$ corresponding to a single pulse. For this plot, Ω_0 was set to 1 THz and σ to 20 ps. The graph is centered around $t_0 = 125$ ps.

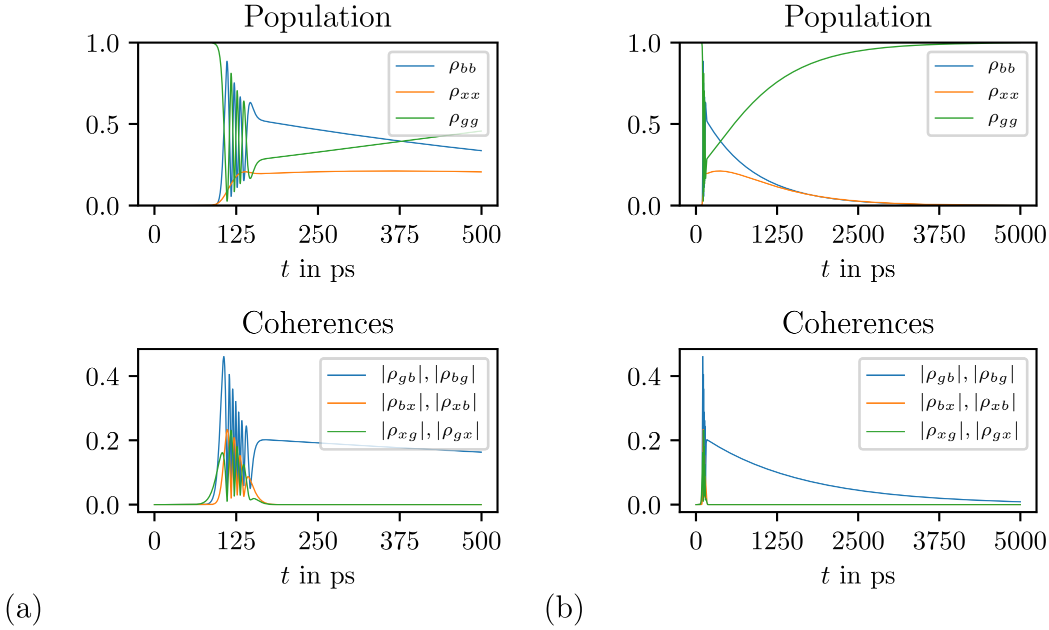

Figure 5.2: Dynamics of the quantum dot density matrix referring to the choice of $\Omega(t)$ as shown in figure 5.1. The diagonal elements are denoted by "Population" and the off-diagonal elements are indicated by "Coherences". n, the exponent of the dephasing rate, was set to 2 for this plot (linear dephasing). Subfigure (b) is the extension of subfigure (a) for a larger time interval.

5.1 Dynamics of the quantum dot

The numerical solution of $\rho_{\text{dot}}(t)$ for an exemplary choice of parameter values is presented in figure 5.2. The quantum dot is initially in the ground state. Rabi oscillations can be observed during the time of the pulse. The biexciton level is populated and decays after the pulse. Exciton population can be observed as well. The off-diagonal elements ρ_{bg} and ρ_{gb} show a significant magnitude.
Figure 5.2b depicts the dynamics of the quantum dot which is shown in figure 5.2a for a larger time interval. The population returns to the ground state after that time span. The coherences show a slower decay compared to the population. For

the theoretical realization of the tomographic method we assume that the quantum dot has returned to the ground state at the arrival of the second or late pulse (see subsection 4.3.2). Jayakumar et al. [2] state that the delay between the early and late pulse is 3.2 ns for their experiment. Taking this time as a reference and looking at the quantum dot's density matrix in figure 5.2b at the time of around 3200 ps however yields that the coherences would not have been completely decayed at the arrival of the second pulse. This suggests that our approximation is limited to a certain regime of time delays, pulse lengths and laser intensities. Figure 5.3 depicts the remaining population and the largest absolute value of the remaining coherences at around 3200 ps for varying Ω_0 and σ. The figure shows alternating regions with fewer and more remaining population and coherences. These regions do not coincide between subfigure (a) and (b). For low values of Ω_0 and σ these areas seem to follow the lines of constant energy per pulse better than for high values. The intensity dependent dephasing might be a reason for that. Both, the values for the remaining population and the largest absolute value of the remaining coherences do not reach the order of 10^{-1}.

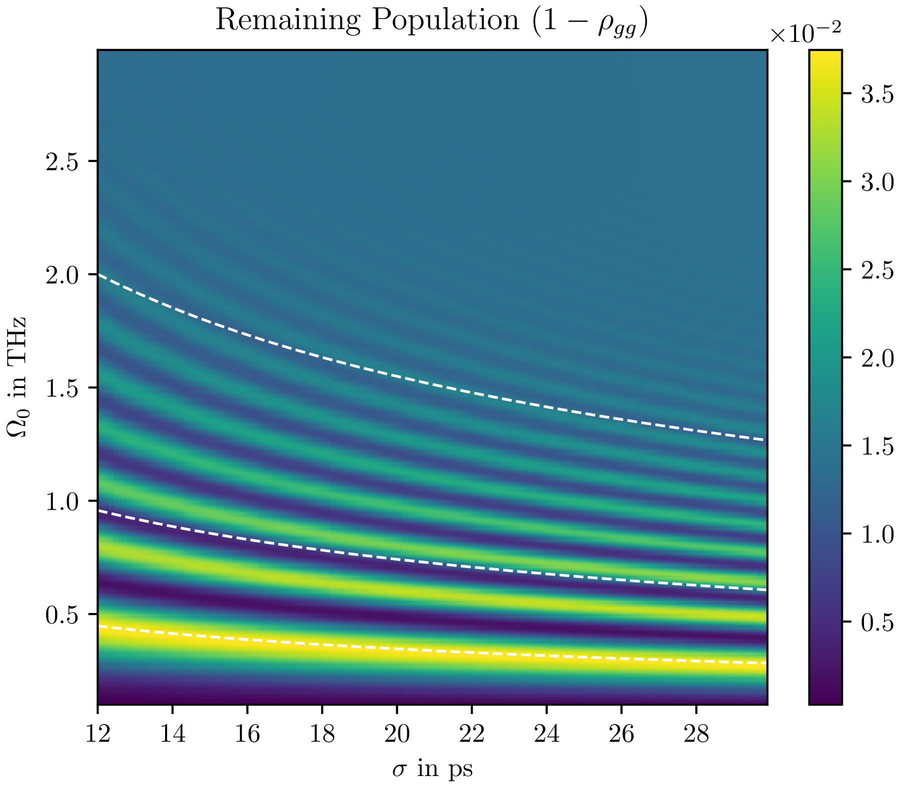

(a)

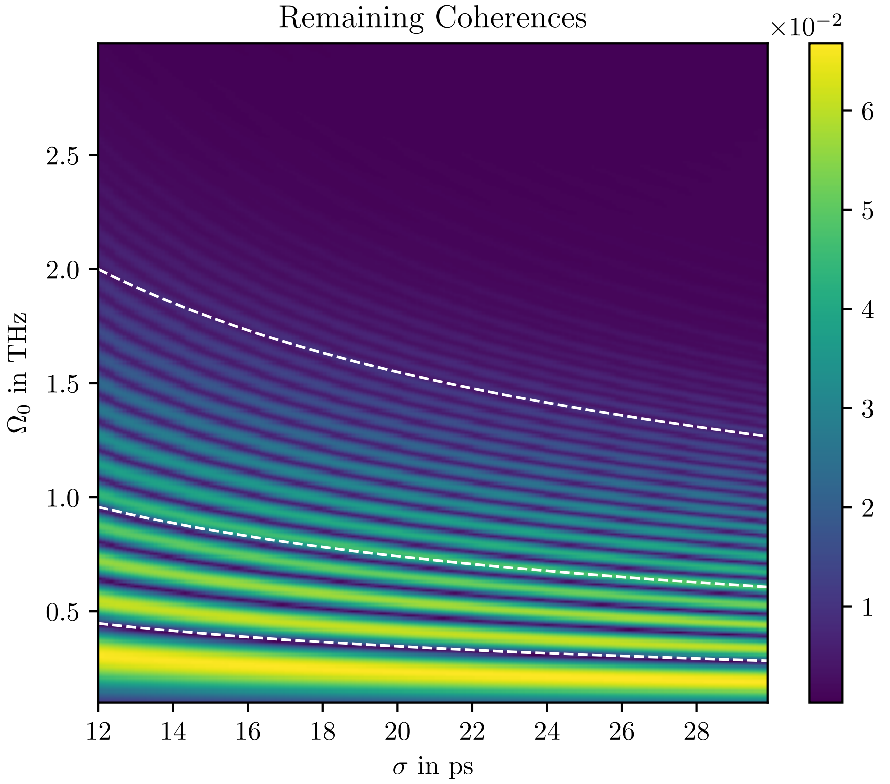

(b)

Figure 5.3: (a): The population calculated as $1-\rho_{gg}$ remaining at a time around 3200 ps. (b): The value of the largest remaining coherence (maximum of $|\rho_{gb}|, |\rho_{bx}|, |\rho_{xg}|$) at this time. The energy per pulse is constant along the dashed white lines. Ω_0 and σ are varried, $\Omega(t)$ is centered at 125 ps and $n = 2$ (linear dephasing). The labels of the colorbar are displayed in the decimal power of -2.

The dynamics of the population and coherences for different values of Ω_0 and σ are depicted in figure 5.4. Strongly weakened coherences after the pulse can be observed in subfigure 5.4a. Compared to figure 5.2, Ω_0 is increased by the factor of 2 for this subfigure. For subfigure 5.4b and 5.4c, Ω_0 was reduced to 0.5 THz. The Rabi oscillations are slowed down and the coherences are increased in comparison to subfigure 5.4a. σ is reduced to 12 ps for subfigure 5.4c. Compared to subfigure 5.4b, this has the effect of an increase in the biexciton population and coherences. Ω_0 is reduced to 0.2 THz in subfigure 5.4d. Here, the coherences are relatively large compared to the population. This leads to a reconstructed density matrix similar to the one of a Bell state as it will be depicted in the next section.

The energy per pulse is proportional to $\Omega_0^2\sigma$ [1]. This quantity is decreased along the subfigures (from subfigure 5.4a to 5.4d). In this work, exemplary lines of constant energy per pulse are plotted as dashed lines in the colorplots with a Ω_0 and σ axis. These lines exhibit a square root behaviour since if $E \propto \Omega_0^2\sigma$ with E being the energy per pulse, a relation for $\Omega_0(\sigma)$ can be given as $\Omega_0(\sigma) \propto \sqrt{\frac{E}{\sigma}}$.

A discussion of the system always has to include both, Ω_0 and σ. For instance, as one can see by going from subfigure 5.4a to subfigure 5.4b and 5.4c reducing Ω_0 could either lead to an increase or decrease of the population, depending on the value of σ. There is no trivial relationship that determines whether certain values of Ω_0 and σ will lead to good results. There is a non trivial relationship between these parameters and the fidelity of the photons' density matrix to a Bell state, which will be discussed in section 5.3.

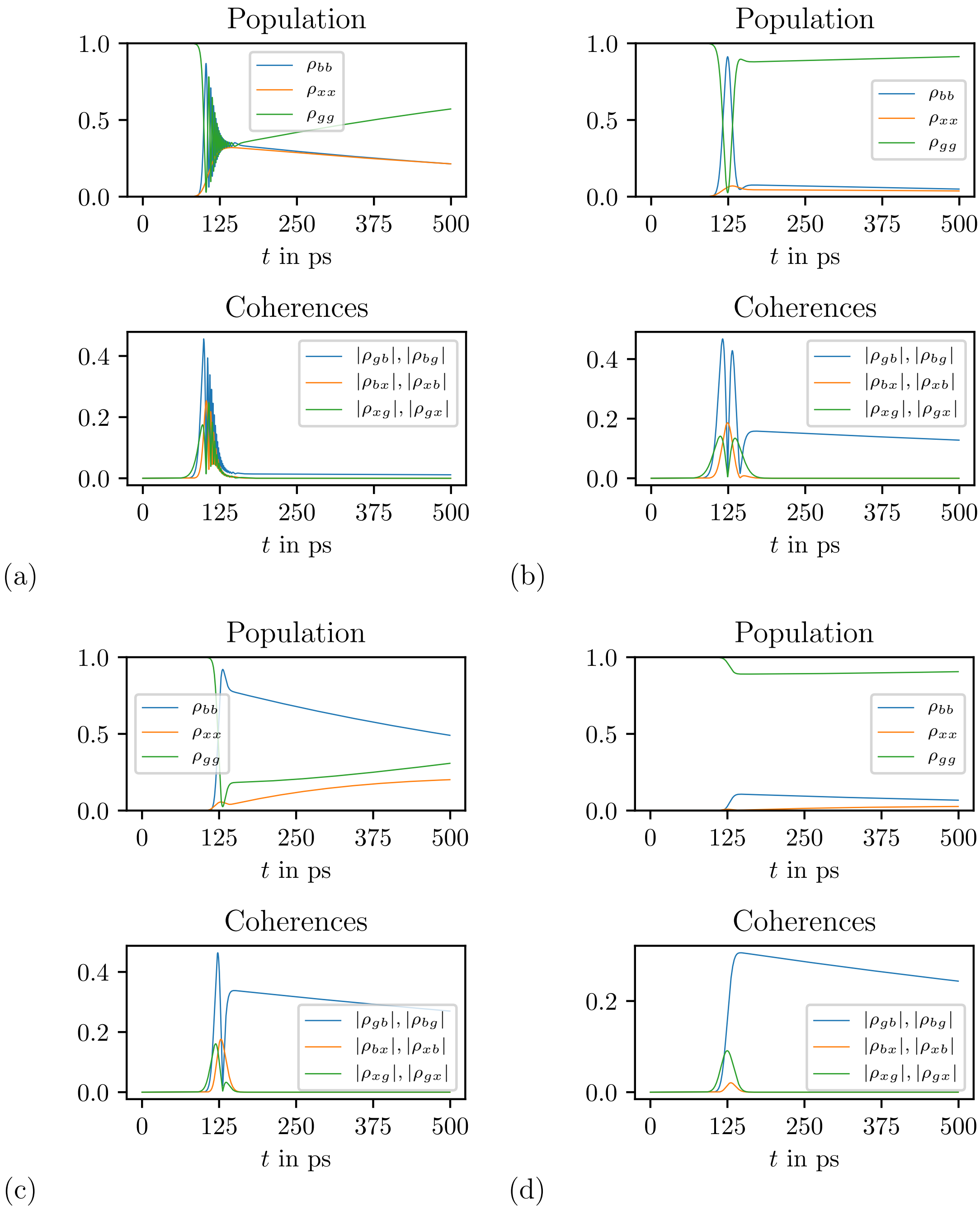

(a) (b) (c) (d)

Figure 5.4: Elements of the quantum dot's density matrix for different values of Ω_0 and σ. $\Omega(t)$ is centered around 125 ps and $n = 2$ (linear dephasing) for every subfigure. (a): $\Omega_0 = 2$ THz, $\sigma = 20$ ps. (b): $\Omega_0 = 0.5$ THz, $\sigma = 20$ ps. (c): $\Omega_0 = 0.5$ THz, $\sigma = 12$ ps. (d): $\Omega_0 = 0.2$ THz, $\sigma = 12$ ps.

5.2 Density matrix of the photons

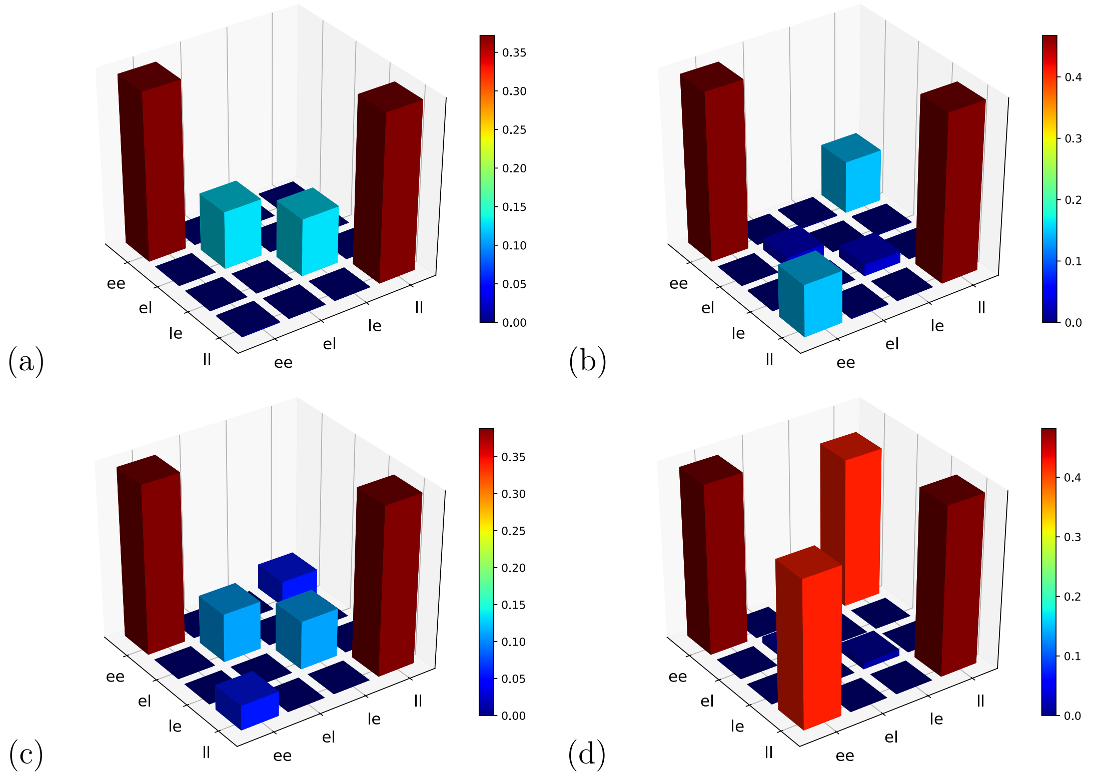

(a) (b) (c) (d)

Figure 5.5: The real part of the reconstructed density matrix ρ_{photons}. The imaginary part is negligibly small. The numerical integral for simulating the number of coincidence counts is taken from 0 to 10000 ps. The center of $\Omega(t)$, the value of n for all subfigures and the value of Ω_0 and σ for every individual subfigure was chosen as in figure 5.4: (a): $\Omega_0 = 2$ THz, $\sigma = 20$ ps. (b): $\Omega_0 = 0.5$ THz, $\sigma = 20$ ps. (c): $\Omega_0 = 0.5$ THz, $\sigma = 12$ ps. (d): $\Omega_0 = 0.2$ THz, $\sigma = 12$ ps.

The goal of the underlying experiment is the preparation of photons such that their reconstructed state is close to a generalized Bell state. Figure 5.5 depicts the theoretically reconstructed density matrix ρ_{photons} for various combinations of Ω_0 and σ. Subfigure 5.5d shows a density matrix similar to the one of the Bell state $|\Phi_0\rangle = \frac{1}{\sqrt{2}}(|\text{ee}\rangle + |\text{ll}\rangle)$. The configuration of parameters chosen for 5.5a leads to a density matrix with vanishing coherences. While the density matrix in subfigure 5.5b and 5.5c show coherences, the matrix elements $\rho_{\text{ee,ee}}$ and $\rho_{\text{ll,ll}}$ are dominant.
The remaining very small imaginary part of the density matrix could either be a consequence of the physical system or a result of numerical inaccuracies. A density matrix that was reconstructed based on experimental results contains an imaginary part, which however is smaller than the real part [1]. The integral to emulate the number of coincidence counts was performed over the time interval from 0 to 10000 ps, which is larger then the time between the early and late pulse chosen by Jayakumar et al. [2], who specify a time span of 3200 ps between the pulses. The time interval of the simulation has been chosen relatively large in order to include potential dynamics on a large time scale. If the theoretical simulation is compared to experimental results this discrepancy has to be taken into account. Due to potential decoherence mechanisms that have not been considered within the theoretical

model yet, the experimental coherence time might be shorter and allow for a smaller delay time between the pulses.

5.3 Fidelity

The fidelity of two states or density matrices is a measure that expresses how similar these states are or, in other words, how well their mathematical representations coincide. For two density matrices ρ_1 and ρ_2 the fidelity is given by [18]

$$\mathrm{F}(\rho_1, \rho_2) = \mathrm{tr}\left(\sqrt{\rho_1^{1/2}\ \rho_2\ \rho_1^{1/2}}\right). \tag{5.2}$$

If one of the states can be expressed as a pure state $|\Phi\rangle$, the fidelity can be written as [18]

$$\mathrm{F}(|\Phi\rangle, \rho) = \sqrt{\langle\Phi|\rho|\Phi\rangle}. \tag{5.3}$$

In this work, expression 5.3 is used to calculate the fidelity between the Bell state $|\Phi_0\rangle = \frac{1}{\sqrt{2}}(|\mathrm{ee}\rangle + |\mathrm{ll}\rangle)$ and the density matrix ρ_{photons}, which is the output of the simulation and tomography. In the following, the fidelity F always refers to this choice of states. F can have values in between 0 and 1, where $\mathrm{F} = 1$ would mean that $\rho_{\mathrm{photons}} = |\Phi_0\rangle\langle\Phi_0|$ and $\mathrm{F} = 0$ if all vectors of ρ_{photons}'s spectral decomposition are orthogonal to $|\Phi_0\rangle$.

The fidelity is a crucial parameter for the analysis of the system under consideration. A discussion of F for different values of system parameters leads to a notion on how these parameters affect ρ_{photons}. As a result we are able to propose certain ranges of Ω_0 and σ that will lead to high fidelities which indicate a reconstructed state that is similar to the bell state $|\Phi_0\rangle$. The density matrix depicted in subfigure 5.5d is a candidate for a high fidelity. In order to discuss the relation between system parameters and the fidelity, colorplots of the fidelity over Ω_0 and σ are shown in figure 5.6. Areas of high fidelity can be observed. This implies that values for Ω_0 and σ exist for which the simulation proposes good measurement results. In other words, the theoretical analysis suggests choices for the laser's parameters that will eventually lead to photons with a reconstructed density matrix that is close to the one of the Bell state $|\Phi_0\rangle = \frac{1}{\sqrt{2}}(|\mathrm{ee}\rangle + |\mathrm{ll}\rangle)$.

The colorplot of the fidelity shows an alternating pattern that follows the dashed white lines in regions of low energy. The accordance between the pattern and white lines seems to be broken for regions of higher pulse energy. A similar structure could already be observed in figure 5.3. This suggests that the energy per pulse might be the crucial parameter that dictates the physics for low energies. This dependency might be broken for higher energies due to the intensity dependent dephasing. By comparing figure 5.6a and 5.6b, it can be observed that the fidelity is slightly more suppressed in regions of higher energy for quadratic dephasing compared to the case of linear dephasing. In order to calculate the fidelity, only the real part of the expression $\langle\Phi_0|\rho|\Phi_0\rangle$ was taken into account here. The imaginary part however is of negligible magnitude and might be the result of numerical inaccuracies. A discussion of the fidelity for other choices of the phase φ of the generalized bell state $|\Phi_\varphi\rangle = \frac{1}{\sqrt{2}}(|\mathrm{ee}\rangle + e^{i\varphi}|\mathrm{ll}\rangle)$ could be added in the future. The density matrix depicted in reference [1] suggests a different choice for φ.

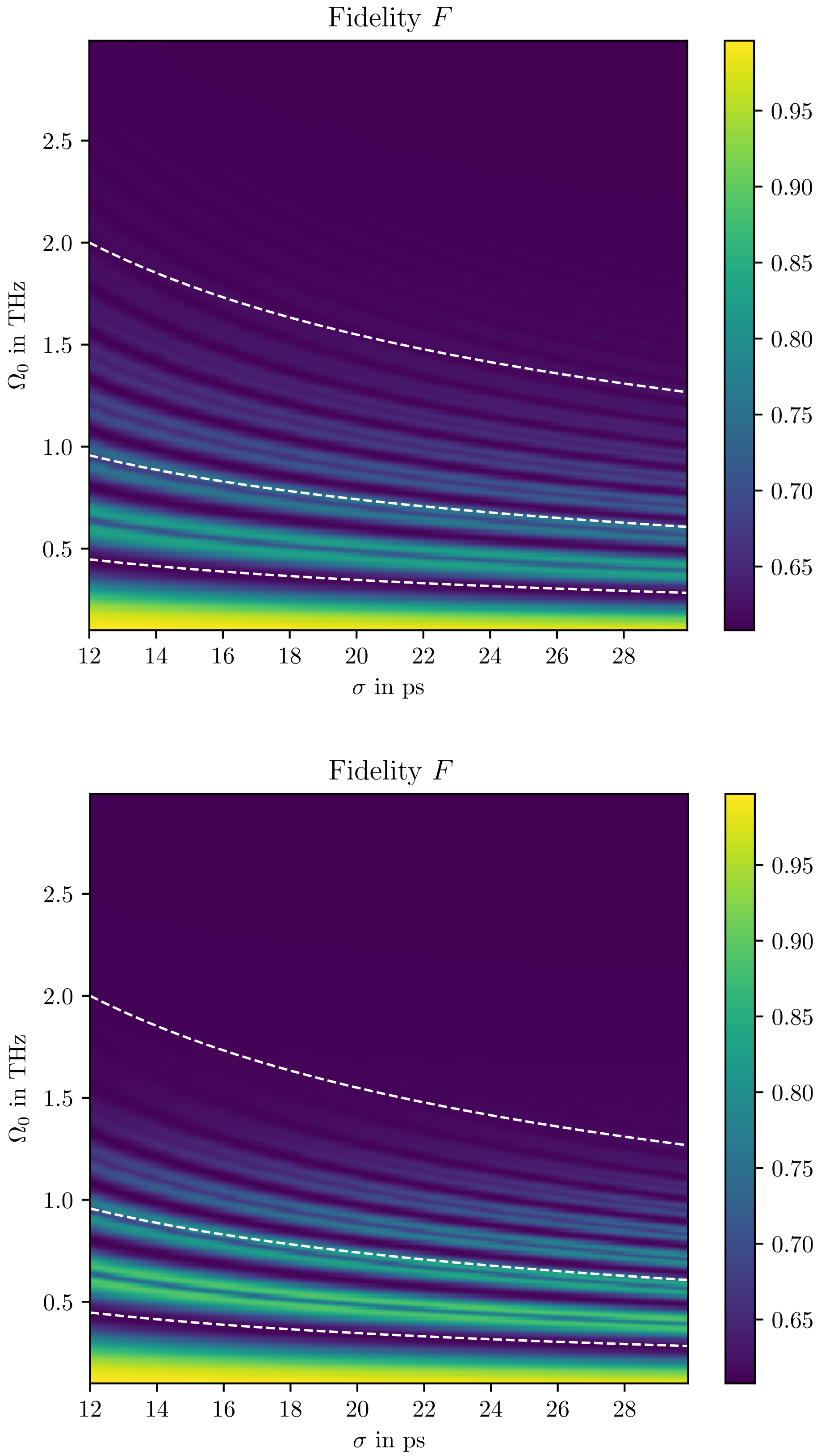

(a)

(b)

Figure 5.6: Colorplot of the fidelity F for various values of Ω_0 and σ. The dashed white lines correspond to lines of constant energy per pulse. $\Omega(t)$ is centered around 125 ps, the integral for the simulation of the number of coincidence counts is evaluated from 0 to 10000 ps. (a): $n = 2$ (linear dephasing). (b): $n = 4$ (quadratic dephasing).

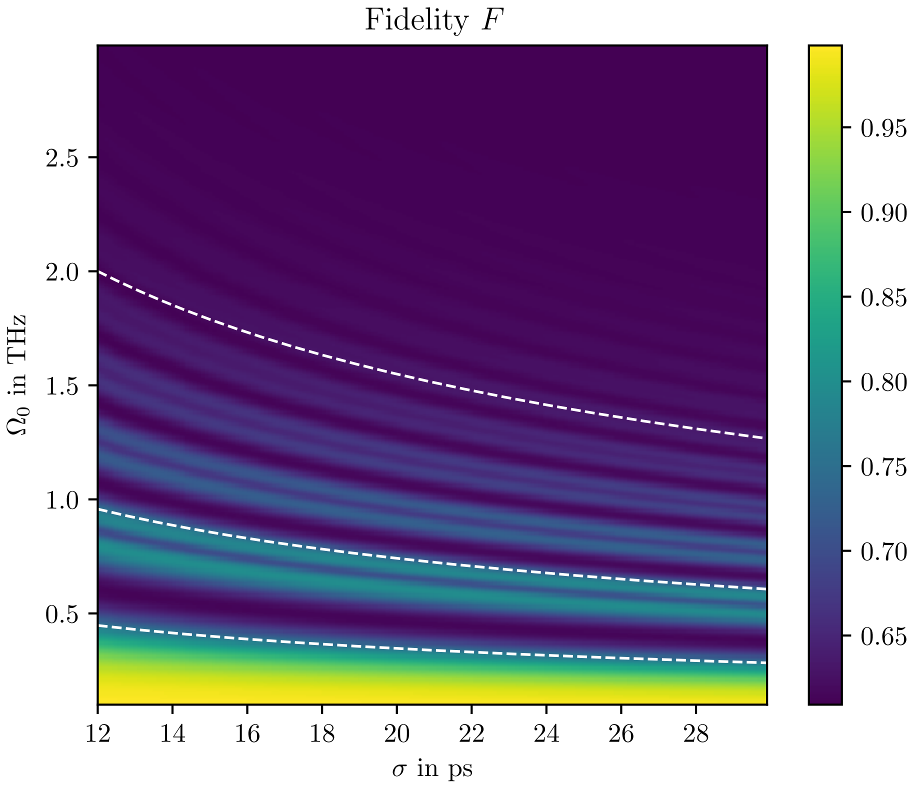

Figure 5.7: Colorplot of the fidelity F for various values of Ω_0 and σ with the value of Δ_x that is derived in equation 5.1. The values for the other parameters were chosen as in figure 5.6a.

As it was illustrated in equation 5.1, it is possible to derive a different value for Δ_x with respect to the value given in table 5.1. Figure 5.7 depicts the fidelity for this alternative choice of Δ_x. This alternative value is approximately the double of the one used for the other figures in this chapter. To allow a comparison, the values for the other parameters have been chosen as in figure 5.6a. Figure 5.7 shows a stretched pattern of the fidelity colorplot, the fundamental behaviour, however, is not changed.

Figure 5.6 and 5.7 depict very high fidelities for regions of low energy. However, only few photons might be created in this region. How many photons are generated might be crucial for a potential application of the system. A discussion of the number of simulated coincidence counts for various values of Ω_0 and σ is presented in the following. Values for the number of simulated coincidence counts are obtained by using relation 4.27. f_ν appears on the right hand side of this relation. Expressions that are proportional to f_ν are given in table 4.1 for all ν. They are a function of the quantum dot's density matrix elements. The values for the matrix elements are the output of the numerical solution of the system's master equation. The integral that is indicated in relation 4.24 is performed numerically from 0 to 10000 ps by using the trapezoidal rule. The results for all 16 configurations of states (see table 4.1) are added up and the resulting numbers are presented in figure 5.8a. Bright areas correspond to a high number of simulated counts and dark regions correspond to few proposed counts. Within this discussion, the real part of the sum is depicted, as the imaginary part is small and a result of numerical inaccuracies, since the values for $f_\nu(t)$ are real from their definition.

The depicted values are proportional to the number of simulated coincidence counts. The values that are indicated by the colorbar are not the exact number of counts, but a reference for the magnitude of the number of counts due to the proportionality. Few coincidence counts are proposed for low energy and an alternating behaviour can be observed when the energy is increased. The system's dominating pattern as in previous plots can be seen. To compare the fidelity and values proportional to the number of coincidence counts, these quantities are scaled to the interval $[0, 1]$ and are subsequently multiplied. The result of this product is depicted in figure 5.8b for various values of Ω_0 and σ. The scaling of the fidelity and values proportional to the number of coincidence counts is done by subtracting all entries of the respective numerical array by the smallest entry and dividing the consequent values by the largest entry of the resulting array. The plot proposes a small overall accordance. Depending on the potential application of the system, different number of counts might be required which eventually leads to the reduction of the fidelity that has to be taken into account in order to assure a necessary number of counts.

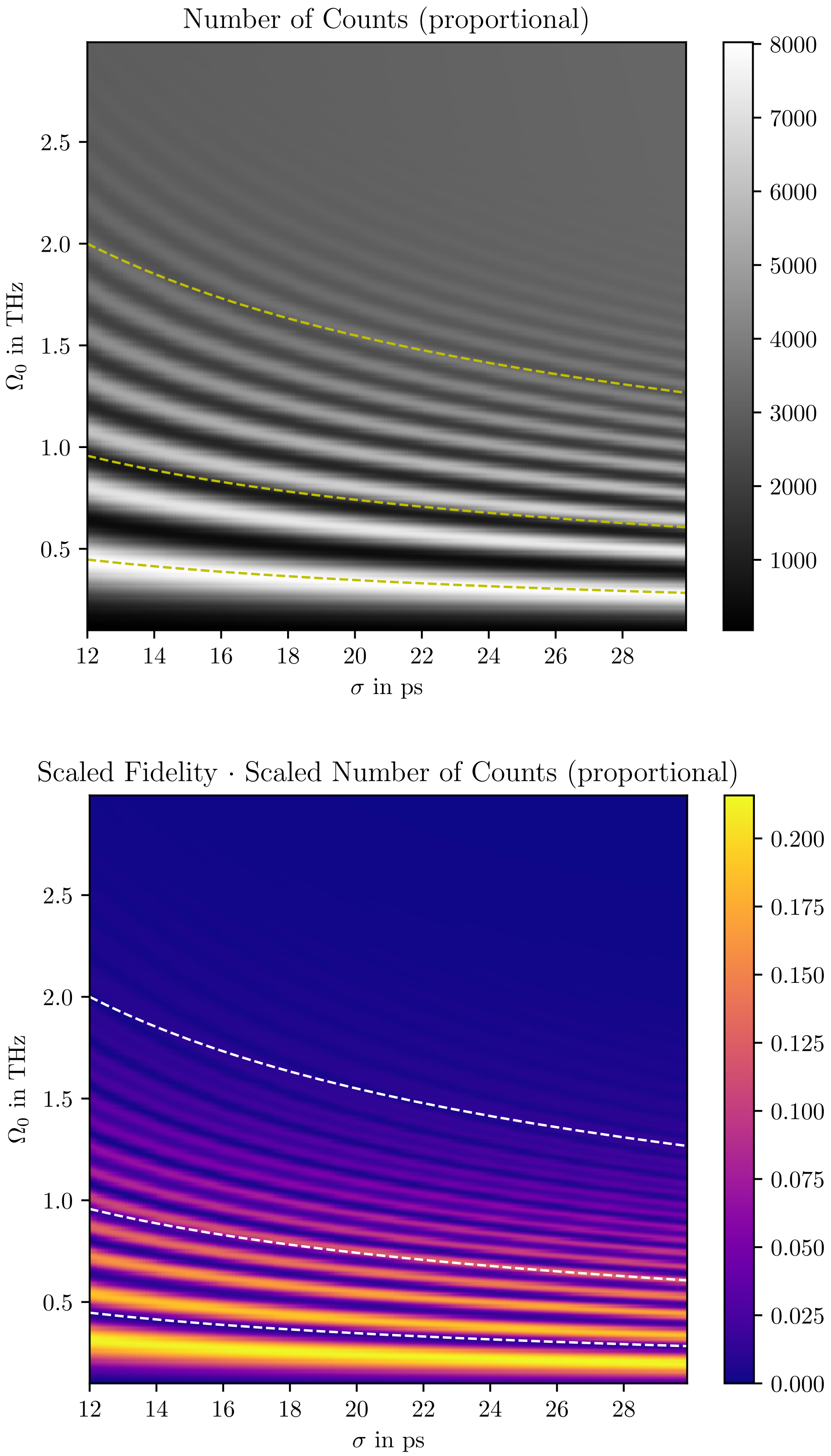

(a)

(b)

Figure 5.8: (a): The sum of the values proportional to the number of coincidence counts n_ν for all 16 configurations of projective measurements. (b): Both, the fidelity which is depicted in figure 5.6a and the number of counts is scaled to the interval $[0, 1]$ and multiplied. Ω_0 and σ are varied. The integral limits and parameters for the computation of the number of coincidence counts are chosen as in figure 5.6a. The dashed lines depict lines of constant energy per pulse.

Chapter 6

Conclusion

This work displays the possibility to run a tomographic method with simulated coincidence counts as an input and thereby reconstruct density matrices of photons in a simulation. With this procedure it is possible to propose the output (the reconstructed density matrix) of the photonic experiment under consideration. Choices for values of Ω_0 and σ, that lead to high fidelities between a bell state and the reconstructed density matrix, can be suggested. Thereby it might be possible to optimize the fidelity by making use of the theoretical analysis in this thesis. However, this requires that the values for Ω_0, σ and the phase φ of the generalized bell state are determined such that the simulation corresponds to the actual dynamics of the experiment.

The theoretical reconstruction of a density matrix by means of the tomographic model is a powerful analysis tool that can be used for other experiments as well.

The analysis of the system proposed a sparse accordance between the fidelity of the reconstructed density matrix and the number of coincidence counts. The latter quantity is related to the number of created photons. This forces the potential user of the system to find a compromise between the quality and the quantity of created photons.

It might be important to scrutinize, whether the entanglement of the photons goes back to the correlation of the pulses hitting the quantum dot or if the entanglement is actually created by the tomographic measurement scheme. This issue can be examined by running the experiment without the schematically first interferometer and analysing the results.

To discuss the fidelity for different phases of the generalized Bell state could be an interesting extension of the analysis. As a next step, the theoretical results of this work have to be thoroughly compared to experimental results. This determines the validity of the theoretical study and might lead to necessary adjustments of the theoretical model, like considering additional decoherence mechanisms. For this purpose, the theoretical results of this work should be extended to regions of lower pulse lengths.

Bibliography

[1] Tobias Huber et al. “Coherence and degree of time-bin entanglement from quantum dots”. In: *Phys. Rev. B* 93 (20 2016), p. 201301. DOI: `10.1103/PhysRevB.93.201301`. URL: `http://link.aps.org/doi/10.1103/PhysRevB.93.201301`.

[2] Harishankar Jayakumar et al. “Time-bin entangled photons from a quantum dot”. In: *Nature Communications* 5 (4251 2014). DOI: `10.1038/ncomms5251`. URL: `http://dx.doi.org/10.1038/ncomms5251`.

[3] Harishankar Jayakumar et al. “Deterministic Photon Pairs and Coherent Optical Control of a Single Quantum Dot”. In: *Phys. Rev. Lett.* 110 (13 2013), p. 135505. DOI: `10.1103/PhysRevLett.110.135505`. URL: `http://link.aps.org/doi/10.1103/PhysRevLett.110.135505`.

[4] J. F. Dynes et al. “Efficient entanglement distribution over 200 kilometers”. In: *Opt. Express* 17.14 (2009), pp. 11440–11449. DOI: `10.1364/OE.17.011440`. URL: `http://www.opticsexpress.org/abstract.cfm?URI=oe-17-14-11440`.

[5] Daniel F. V. James et al. “Measurement of qubits”. In: *Phys. Rev. A* 64 (5 2001), p. 052312. DOI: `10.1103/PhysRevA.64.052312`. URL: `http://link.aps.org/doi/10.1103/PhysRevA.64.052312`.

[6] Hiroki Takesue and Yuita Noguchi. “Implementation of quantum state tomography for time-bin entangled photon pairs”. In: *Opt. Express* 17.13 (2009), pp. 10976–10989. DOI: `10.1364/OE.17.010976`. URL: `http://www.opticsexpress.org/abstract.cfm?URI=oe-17-13-10976`.

[7] Manfred Sigrist. *Lecture Notes: Solid State Theory.* `http://edu.itp.phys.ethz.ch/fs14/sst/Lecture-Notes.pdf`. Institute for Theoretical Physics, ETH Zürich, Spring Semester 2014. Accessed: 24 January 2017.

[8] Richard W. Robinett. *Quantum Mechanics: Classical Results, Modern Systems, and Visualized Examples.* Second Edition. Oxford University Press, 2006.

[9] David W. Snoke. *Solid state physics: essential concepts.* Addison-Wesley, 2009.

[10] Florian Marquardt and Annett Püttmann. *Introduction to dissipation and decoherence in quantum systems.* arXiv:0809.4403v1, `https://arxiv.org/pdf/0809.4403.pdf`. 2008.

[11] Oriol Romero-Isart. *Lecture Notes: Quantum Optics.* Lecture Title: “Theoretische Quantenoptik und Quanteninformation”, University of Innsbruck, Summer Semester 2015.

[12] Wolfgang Demtröder. *Laser Spectroscopy, Vol. 1: Basic Principles.* Fourth Edition. Springer-Verlag Berlin Heidelberg, 2008.

[13] Daniel A. Steck. *Quantum and Atom Optics*. available online at `http://steck.us/teaching`. (revision 0.11.6, 24 February 2017).

[14] Roy J. Glauber. "The Quantum Theory of Optical Coherence". In: *Phys. Rev.* 130 (6 1963), pp. 2529–2539. DOI: `10.1103/PhysRev.130.2529`. URL: `https://link.aps.org/doi/10.1103/PhysRev.130.2529`.

[15] J.R. Johansson, P.D. Nation, and Franco Nori. "QuTiP: An open-source Python framework for the dynamics of open quantum systems". In: *Computer Physics Communications* 183.8 (2012), pp. 1760–1772. DOI: `http://dx.doi.org/10.1016/j.cpc.2012.02.021`. URL: `http://www.sciencedirect.com/science/article/pii/S0010465512000835`.

[16] J. D. Hunter. "Matplotlib: A 2D graphics environment". In: *Computing In Science & Engineering* 9.3 (2007), pp. 90–95. DOI: `10.1109/MCSE.2007.55`.

[17] Aaron Meurer et al. "SymPy: symbolic computing in Python". In: *PeerJ Computer Science* 3 (Jan. 2017), e103. DOI: `10.7717/peerj-cs.103`. URL: `https://doi.org/10.7717/peerj-cs.103`.

[18] Michael A. Nielsen and Isaac L. Chuang. *Quantum Computation and Quantum Information*. 10th Anniversary Edition. Cambridge University Press, 2010.